MIT Open Access Articles

Seismic investigation of the transition from continental to oceanic subduction along the western Hellenic Subduction Zone

Massachusetts Institute of Technology

Seismic investigation of the transition from continental to oceanic subduction along the western Hellenic Subduction Zone

F. D. Pearce,[1] S. Rondenay,[2] M. Sachpazi,[3] M. Charalampakis,[3] and L. H. Royden[1]

[1]   The western Hellenic subduction zone (WHSZ) exhibits well-documented along-strike variations in lithosphere density (i.e., oceanic versus continental), subduction rates, and overriding plate extension. Differences in slab density are believed to drive deformation rates along the WHSZ; however, this hypothesis has been difficult to test given the limited seismic constraints on the structure of the WHSZ, particularly beneath northern Greece. Here, we present high-resolution seismic images across northern and southern Greece to constrain the slab composition and mantle wedge geometry along the WHSZ. Data from two temporary arrays deployed across Greece in a northern line (NL) and southern line (SL) are processed using a 2D teleseismic migration algorithm based on the Generalized Radon Transform. Images of P- and S-wave velocity perturbations reveal N60E dipping low-velocity layers beneath both NL and SL. The ~8 km thick layer beneath SL is interpreted as subducted oceanic crust while the ~20 km thick layer beneath NL is interpreted as subducted continental crust. The thickness of subducted continental crust inferred within the upper mantle suggests that ~10 km of continental crust has accreted to the overriding plate. The relative position of the two subducted crusts implies ~70–85 km of additional slab retreat in the south relative to the north. Overall, our seismic images are consistent with the hypothesis that faster sinking of the denser, oceanic portion of the slab relative to the continental portion can explain the different rates of slab retreat and deformation in the overriding plate along the WHSZ.

1.   Introduction

[2]   The Hellenic subduction system provides a natural laboratory for exploring the relationship between slab density, subduction rate, and overriding plate deformation. Extensive GPS studies have documented rapid subduction along southern Greece (~35 mm/yr) and slow subduction (5–8 mm/yr) along northern Greece (Figure 1a) [*McClusky et al.*, 2000; *Hollenstein et al.*, 2008]. Marine seismic data have shown that the foreland of the northern Hellenides consists of continental lithosphere [*Finetti and Del Ben*, 2005], whereas the foreland of southern Greece, beneath the Ionian Sea, is of oceanic lithosphere affinity [*Finetti et al.*, 1991; *de Voogd et al.*, 1992]. Thus, the Western Hellenic Subduction Zone (WHSZ) can be separated into northern and southern

segments, each with a different convergence rate and slab composition [*Papanikolaou and Royden*, 2007]. These segments are dextrally offset by ~100 km along the Cephalonia transform fault, which has recently (~1–4 Ma) linked with the North Anatolian fault system through a broad region of extensional and strike-slip faults known as the Central Hellenic Shear Zone [*Papanikolaou and Royden*, 2007; *Reilinger et al.*, 2010; *Vassilakis et al.*, 2011].

[3]   Numerous tectonic models have been proposed to explain the large variations in convergence rate and overriding plate deformation along the western Hellenic subduction zone. Such models generally appeal to two large-scale tectonic forces: (1) the westward extrusion of Anatolia driven by Arabia collision [*McKenzie*, 1972; *Sengor et al.*, 1985] and (2) the southwestward pull of the subducting Ionian lithosphere along the southern segment [*Le Pichon and Angelier*, 1979; *Royden*, 1993]. The importance of rapid trench retreat along the southern segment has been shown through GPS studies (i.e., larger, southerly velocity of the Aegean block compared to Anatolia) and models that explain the pattern of extension in the overriding plate [*Meijer and Wortel*, 1996; *Gautier et al.*, 1999; *McClusky et al.*, 2000]. In contrast, slow convergence along the northern segment has been attributed to the resistance offered by the positively buoyant continental lithosphere to being subducted [*Taymaz et al.*, 1991], a resistance that may have led to its

---

[1]Department of Earth, Atmospheric, and Planetary Sciences, Massachusetts Institute of Technology, Cambridge, Massachusetts, USA.
[2]Department of Earth Science, University of Bergen, Bergen, Norway.
[3]Geodynamic Institute, National Observatory of Athens, Athens, Greece.

Corresponding author: F. D. Pearce, Department of Earth, Atmospheric, and Planetary Sciences, Massachusetts Institute of Technology, Cambridge, MA 02139, USA. (fpearce@mit.edu)
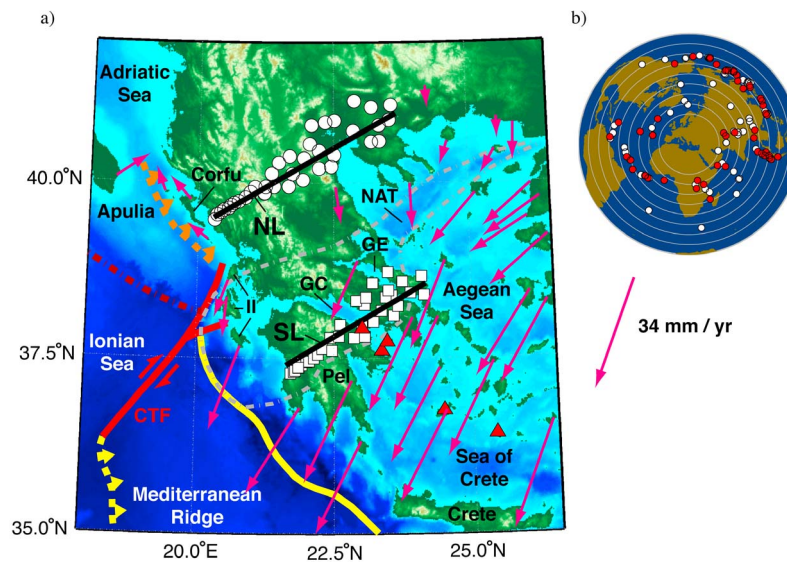
Figure 1. Map of the study area and distribution of teleseismic events used in our analysis. (a) Map of the Western Hellenic subduction zone. Yellow lines show the active, southern segment boundaries: thrust front of the Mediterranean ridge (dashed) and trench (solid). Dashed orange line shows thrust front of northern segment. Bright red line denotes the Cephalonia transform fault (CTF) and dark red dotted line marks the Apulian Escarpment (i.e., the oceanic-continental transition). Dashed gray line outlines the North Aegean trough (NAT) and the central Hellenic shear zone. GPS velocities (magenta arrows) relative to Eurasia are from *McClusky et al.* [2000]. Seismic stations deployed across southern and northern Greece are denoted by white squares and circles, respectively. The surface projection of our two 2D-GRT profiles are denoted by thick black lines (SL and NL). Additional acronyms: II, Ionian Islands (Cephalonia in middle); GC, Gulf of Corinth; GE, Gulf of Evia; Pel, Peloponnesus. (b) Distribution of events used in teleseismic migration of SL (red circles) and NL (white circles). Map is centered between the two arrays with white concentric circles denoting 10° increments in epicentral distance (innermost circle at 30°).

separation from the rapid subduction regime south of the Cephalonia transform fault [e.g., *Kahle et al.*, 2000; *Royden and Papanikolaou*, 2011]. Recent numerical and experimental models have also shown that variations in slab density play an important role in driving slab rollback and overriding plate motion [*Brun and Faccenna*, 2008; *Husson et al.*, 2009; *Faccenna and Becker*, 2010; *Chemenda et al.*, 1996; *Bialas et al.*, 2011].

[4] The transition between the northern and southern segments of the WHSZ has been the focus of intense study, as it is one of the most seismically active regions in Europe. At shallow depths, the Cephalonia transform fault defines the northern limit of rapid subduction along the WHSZ; however, the nature of the separation between the two segments at depth is highly debated. Numerous authors have suggested a trench-parallel slab tear may be propagating from north to south along the WHSZ in response to progressive continental collision [*Wortel and Spakman*, 2000, and references therein]. The Cephalonia transform fault has also been proposed as the surface manifestation of a vertical tear in the lithosphere, termed a Subduction-Transform Edge Propagator, which separates the northern and southern segments at depth [*Govers and Wortel*, 2005]. More recently, *Suckale et al.* [2009] suggest that a trench-perpendicular tear in the subducted slab beneath the Central Hellenic Shear Zone may have developed along the boundary between oceanic and continental lithosphere. Based on geodynamic modeling, *Royden and Papanikolaou* [2011] argue that the recent entry

of denser, oceanic lithosphere into the southern segment has produced faster trench retreat, leading to the segmentation of the WHSZ along the Cephalonia transform fault as shown in Figure 2. It is not known how the differential slab retreat may be accommodated at greater depth (D > 30 km), perhaps through bending and/or tearing. Such subduction models have been difficult to test, as most seismic studies have focused on the active, southern segment, with only limited constraints available on the structure of the subduction boundary along the northern segment.

[5] The objective of this study is to better constrain the transition from the northern to southern segment of the WHSZ through detailed imaging of the subducted slab in both regions. To do so, we deployed two high-density seismic arrays across northern and southern Greece (Figure 1a), as a part of the Multidisciplinary Experiments for Dynamic Understanding of Subduction under the Aegean Sea (MEDUSA) project. Here, we present and discuss high-resolution images obtained by 2-D teleseismic migration of the data recorded by these arrays. The seismic images introduce new, independent evidence that continental crust is subducting below northern Greece, in contrast to the oceanic crust subducting beneath the Peloponnesus in the south. The relative position of the two segments suggests 70–85 km of additional trench retreat may have occurred along the southern segment compared to the northern segment, thereby providing a simple mechanism that can explain the majority of the ~100 km offset along the Cephalonia transform fault.
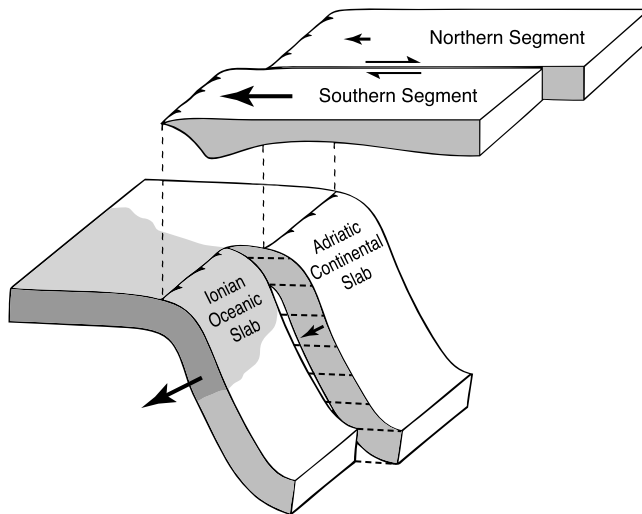
Figure 2. Schematic diagram showing the hypothesized geometry of a segmented slab in the Hellenic subduction zone, modified from *Royden and Papanikolaou* [2011]. There may be either a tear, as depicted, or a smooth ramp between the Adriatic and Ionian slabs (in the region containing horizontal dashed lines).

Thus, our results provide important new constraints on the composition and geometry of the subducted lithosphere along the WHSZ.

2. Geological Setting

[6] The Hellenic subduction zone defines the boundary between the slowly converging African and Eurasian plates within the central Mediterranean region (Figure 1a). The western portion of the Hellenic subduction zone has a length of approximately 1000 km trending northwest from the central Adriatic Sea to the west coast of Crete. In this section, we review the geological and geophysical constraints on the southern segment, the northern segment, the Cephalonia transform fault, and the overriding plate.

2.1. Southern Segment

[7] The oceanic crust beneath the Ionian Sea is probably Triassic or Jurassic in age and consists of approximately 5–8 km of igneous crust overlain by 6–10 km of sedimentary cover [*Makris*, 1985; *de Voogd et al.*, 1992; *Kopf et al.*, 2003; *Finetti and Del Ben*, 2005]. Gravity anomalies imply a very dense, negatively buoyant slab within the upper 100–200 km of the southern segment, consistent with the subduction of old oceanic lithosphere [*Royden*, 1993; *Tsokas and Hansen*, 1997]. Pliocene–Quaternary arc volcanoes are located ~200 km north and east of the present-day Hellenic trench (Figure 1a) [*Fytikas et al.*, 1976; *Pe-Piper and Piper*, 2007]. Thrust faults and folds occur within the accretionary prism outboard of the trench, over a width of several hundred kilometers to the front of the Mediterranean ridge [*Kopf et al.*, 2003].

2.2. Northern Segment

[8] The continental crust beneath the southern Adriatic Sea is continental or transitional in character, with a crustal thickness of 25–30 km [e.g., *Morelli et al.*, 1975; *Marone et al.*, 2003; *Cassinis et al.*, 2003; *Finetti and Del Ben*, 2005]. The active thrust front of the northern segment lies just west of the Greek coastline, near the island of Corfu and between the island of Paxos and mainland Greece [*Monopolis and Bruneton*, 1982; *Finetti and Del Ben*, 2005; *Vassilakis et al.*, 2011]. There is no expression of a trench in the bathymetry along the northern segment, but gravity data indicate that the basement is flexed downward beneath the thrust front and that the resulting depression is filled with sedimentary foredeep deposits [*Moretti and Royden*, 1988]. The southern boundary between Apulian continental crust and Ionian oceanic crust occurs along the Apulian escarpment, which is marked by an abrupt change in water depth and Permian-Triassic rift faults (Figure 1a) [*Finetti and Del Ben*, 2005].

2.3. Cephalonia

[9] The Cephalonia transform fault separates the northern and southern segments of the western Hellenic subduction zone [e.g., *Dewey and Şengör*, 1979; *Finetti*, 1982; *Kahle and Mueller*, 1998; *Kahle et al.*, 1995; *Hollenstein et al.*, 2008]. Focal solutions from earthquakes located along the Cephalonia transform fault show right-lateral slip on steeply dipping, southwest-striking fault planes and also thrust faulting on northeast-striking fault planes [*Royden and Papanikolaou*, 2011]. The WHSZ appears to be dextrally offset by ~100 km across the Cephalonia transform fault; however, the precise offset is difficult to determine given the distributed network of faults and block rotations along the south side of the transform [*Vassilakis et al.*, 2011]. The Cephalonia transform fault extends to the northeast into mainland Greece to merge with the broadly defined zone of dextral and extensional deformation in the Central Hellenic Shear Zone (Figure 1a) [*Roberts and Jackson*, 1991; *Armijo et al.*, 1996; *Goldsworthy et al.*, 2002; *Papanikolaou and Royden*, 2007; *Vassilakis et al.*, 2011].

2.4. Overriding Plate

[10] The overriding plate of the WHSZ consists of subduction-related thrust units that have been subjected to variable modes of extension over time. From the Oligocene to the late Miocene, upper plate extension was generally arc-perpendicular in response to a regime similar to back-arc spreading – though one that encompassed both synarc and forearc domains [*Mercier et al.*, 1989; *Papanikolaou*, 1993]. Extension began to focus in the overriding plate of the southern segment in the Late Miocene to Early Pliocene [*Papanikolaou and Royden*, 2007]. Since the Late Pliocene, extension has been concentrated along a series of normal faults oriented approximately E-W and crosscutting older arc-parallel structures. Currently, E-W faults along the Gulf of Corinth and Gulf of Evia accommodate most of the extension in central Greece [*McClusky et al.*, 2000]. Extension in northern Greece has remained arc-parallel but has been much slower since the Late Miocene [*Meyer et al.*, 2002]. This contrast in extension regime between the northern and southern segments has been attributed to an acceleration of the rate of motion of the Hellenic trench to the south of Cephalonia in late Miocene time, in response to a transition to negatively buoyant oceanic lithosphere in that region [e.g., *Papanikolaou and Royden*, 2007]. This

dichotomy has led to considerable differences in crustal thickness of the overriding plate between the northern and southern segments, which have been documented through various seismic studies described in the next section.

2.5. Constraints From Previous Seismic Investigations

[11] A variety of seismic studies have been undertaken in the past decades to image the Hellenic subduction zone. These include traveltime tomography [*Ligdas et al.*, 1990; *Spakman et al.*, 1993; *Papazachos and Nolet*, 1997; *Piromallo and Morelli*, 2003; *Schmid et al.*, 2006], marine reflection and refraction profiles [*Hirn et al.*, 1996; *Mascle and Chaumillon*, 1998; *Clément et al.*, 2000; *Bohnhoff et al.*, 2001; *Kopf et al.*, 2003; *Kokinou et al.*, 2003, 2005], receiver-function analyses [*Knapmeyer and Harjes*, 2000; *Tiberi et al.*, 2001; *Li et al.*, 2003; *van der Meijde et al.*, 2003; *Endrun et al.*, 2005; *Sodoudi et al.*, 2006; *Zhu et al.*, 2006; *Gesret et al.*, 2010], surface-wave dispersion [*Calcagnile et al.*, 1982; *Martínez et al.*, 2001; *Pasyanos and Walter*, 2002; *Meier et al.*, 2004; *Bourova et al.*, 2005; *Karagianni et al.*, 2005; *Di Luccio and Pasyanos*, 2007; *Endrun et al.*, 2008], and seismic anisotropy measurements [*Hearn*, 1999; *Schmid et al.*, 2004]. Here, we review the results from these previous seismic studies, focusing on the insight they provide on the Moho of the overriding plate and subducting slab.

[12] The Moho of the overriding plate has been the subject of several regional investigations across the Gulf of Corinth [*Tiberi et al.*, 2000, 2001; *Clément et al.*, 2004; *Zelt et al.*, 2005], central Greece [*Sachpazi et al.*, 2007], and the Aegean region [*Marone et al.*, 2003; *Tirel et al.*, 2004]. Traveltime tomography and receiver function results from these investigations indicate that the depth of the continental Moho ranges from 20 to 45 km. Depths in excess of 40 km are found beneath the Hellenides in the Peloponnesus and mainland Greece, and are attributed to isostatic compensation of surface relief [*Tiberi et al.*, 2000; *Marone et al.*, 2003]. Shallower Moho depths (<30 km) are found beneath the eastern Gulf of Corinth and the Aegean Sea, with the shallowest depths (<25 km) below the North Aegean Trough and the Sea of Crete [*Tirel et al.*, 2004; *Zelt et al.*, 2005; *Sodoudi et al.*, 2006]. *Sachpazi et al.* [2007] document a line striking SW–NE from the western Gulf of Corinth to the North Aegean Trough as marking the boundary between a domain of thinned crust (~20–35 km) to the southeast (eastern Peloponnesus, Attiki Peninsula, Evia) and one of thicker crust (>35 km) beneath central and northern Greece. In general, the Moho of the overriding plate in northern Greece is more poorly constrained than in the south due to the limited seismic station coverage in this region.

[13] The nature of the foreland slab, as seen prior to reaching the trench, has been constrained primarily by marine reflection and refraction profiles. In the southern segment, such profiles indicate that the crust beneath the Ionian Sea is likely oceanic in origin, with an estimated thickness ranging between 5 km [*Finetti et al.*, 1991; *Finetti and Del Ben*, 2005] and 8 km [*de Voogd et al.*, 1992]. The thickness of the overlying sediments varies greatly from 4 to 6 km west of the deformation front to up to 10 km in the accretionary prism [*Hirn et al.*, 1996; *Mascle and Chaumillon*, 1998; *Bohnhoff et al.*, 2001; *Kopf et al.*, 2003; *Kokinou et al.*, 2003]. East of the trench, detailed active source studies in the Ionian Islands have identified a landward dipping reflector of variable topography at 13 km depth, which is interpreted as the interplate boundary of the subduction zone [*Hirn et al.*, 1996; *Clément et al.*, 2000]. In the northern segment, a recent series of marine seismic lines across Apulia give a detailed picture of the foreland crust currently entering the subduction system. In particular, the M-34 seismic line [*Finetti and Del Ben*, 2005] represents a near-parallel extension of the northern land-based profile presented in this study (see sections 4 and 6.1.2), starting ~25 km to the west of the coast. The interpreted M-34 line shows that the undeformed continental crust entering the thrust front has ~8 km of sedimentary rocks, ~12 km of crystalline upper crust, ~7 km of lower crust and a Moho depth of ~28 km (considering a water depth of ~1 km). As we shall see, these marine seismic data provide critical constraints for the interpretation of our seismic images beneath mainland Greece.

[14] To date, the structure of the WHSZ at depth has been constrained primarily by seismic traveltime tomography at global scale [*Ligdas et al.*, 1990; *Spakman et al.*, 1993; *Karason*, 2002; *Piromallo and Morelli*, 2003] and regional scale [*Papazachos and Nolet*, 1997; *Tiberi et al.*, 2000]. These tomographic models show the subducted slab as a tabular, high-velocity anomaly dipping to the NE beneath the western Hellenic subduction zone. Global models show that the fast anomaly extends well below the transition zone at 660 km, indicating slab penetration into the lower mantle [*van der Hilst et al.*, 1997]. At regional scale, there is evidence for a sudden increase in subduction angle between 70 and 90 km depth beneath the Gulf of Corinth [*Papazachos and Nolet*, 1997; *Tiberi et al.*, 2000; *Sodoudi et al.*, 2006]. The distribution of earthquake hypocenters outlines a diffuse Wadati–Benioff zone that abruptly increases its dip at 90–100 km [*Papazachos et al.*, 2000]. Some tomographic models show the northeast dipping velocity anomaly appears to be weaker north of the Cephalonia transform fault [e.g., *Wortel and Spakman*, 2000] and has a lateral disruption beneath the Cephalonia transform fault [*Suckale et al.*, 2009; *Hosa*, 2008]. These observations have been interpreted as evidence for possible slab detachment in this area [*Spakman et al.*, 1988; *Carminati et al.*, 1998; *Wortel and Spakman*, 2000]. In contrast, P and S receiver functions by *Sodoudi et al.* [2006] show a continuous Moho of the subducting lithosphere beneath northern and southern Greece between 40 and 220 km depth while *Zelt et al.* [2005] observed a reflection from the subducted slab beneath the western Gulf of Corinth at approximately 75 km depth. Thus, the available seismic evidence suggests a continuous slab above ~200 km depth with a possible slab tear beneath the Cephalonia transform fault at greater depths.

[15] A high-resolution seismic profile of the southern segment based on migrated teleseismic scattered waves was recently presented by *Suckale et al.* [2009]. Their image shows the subducted crust as a dipping low-velocity layer extending from 40 km depth beneath the west coast of the Peloponnesus to at least 80 km depth beneath the Isthmus of Corinth. The observed low-velocities are attributed to hydrated metabasalts in the oceanic crust, and the reduction in signal beyond 80 km depth suggests progressive dehydration-eclogitization of these rocks. The data used by *Suckale et al.* [2009] are reanalyzed in this paper, in conjunction with the data collected above the northern

segment, to produce consistent images of the southern and northern segments that will be readily amenable to comparison.

3. Methods

[16] The imaging method used in this study migrates scattered signals in the coda of teleseismic P waves recorded by dense arrays of broadband seismographs to identify discontinuities in material properties within the subsurface [*Bostock et al.*, 2001; *Shragge et al.*, 2001; *Rondenay et al.*, 2001]. It assumes that the scattered wavefield is generated by volumetric perturbations in P- ($\delta\alpha/\alpha$) and S-wave velocities ($\delta\beta/\beta$) within a smoothly varying background velocity model. Preprocessing of the raw data (total wavefield) to isolate the scattered wavefield is critical to forming a high-quality image. The following sections briefly describe the data preprocessing algorithm and the imaging method used in this study.

3.1. Preprocessing

[17] A multichannel approach similar to that of *Bostock and Rondenay* [1999] is employed to isolate the scattered wavefield from the total recorded wavefield. Such multichannel schemes are favored over single-station deconvolution because they provide a more robust estimate of the incident wavefield and thus more stable deconvolved waveforms to higher frequencies. The approach involves the following steps (see *Rondenay et al.* [2005] for details): (1) transform recorded wavefield from N-E-Z to upgoing P-SV-SH using the free-surface transfer matrix [*Kennett*, 1991]; (2) apply multichannel cross-correlation [*VanDecar and Crosson*, 1990] to align the wavefield with respect to the incident P wave; (3) obtain the incident wavefield from the first principal component of the P wavefield; (4) deconvolve the incident wavefield from each residual component to produce an estimate of the normalized scattered wavefield.

[18] In this study, several improvements have been made to the preprocessing workflow described above. First, the longest possible incident wavefield signals (up to ~180 s) are used to ensure that source-side scattering is included in the estimate of the incident wavefield. Second, several iterations over preprocessing steps 2 to 4 are performed to precisely align the scattered wavefield relative to the incident P wave. Last, in the deconvolution step, an optimal damping parameter (i.e., water level) is independently determined for each station component – as opposed to using ad hoc, uniform damping across all components. We chose the smallest damping value such that unstable oscillation is restricted below a prescribed energy threshold (in our case ~0.01% of the undamped energy). If this rather stringent criterion is not met, then the damping is fixed at 5% of the peak in the source wavelet's power spectrum. This procedure reduces overdamping and excessive low-pass filtering of the scattered wavefield. In summary, these improvements yield an input scattered signal that is better aligned along the incident P wave and more stable than that obtained by the traditional workflow of *Rondenay et al.* [2005].

3.2. Teleseismic Migration

[19] The teleseismic migration approach used here assumes single scattering from 2-D line scatterers embedded in a smoothly varying 1-D background model [*Bostock et al.*,

2001]. The approach is based on the Generalized Radon Transform (GRT) and its inverse, and is thus commonly referred to as the 2-D GRT inversion [*Rondenay et al.*, 2005]. The inverse problem can be viewed as a weighted diffraction stack over all sources and receivers that yields an estimate of the scattering potential at a given point in the subsurface, with the weights determined by the analogy between the forward-scattering equation and the GRT [see, e.g., *Miller et al.*, 1987]. The scattering potential is then linearly inverted for velocity perturbations at this point [*Rondenay et al.*, 2005]. The inverse problem is solved for all points in model space to obtain a 2D image of velocity perturbations. For a full theoretical derivation of the 2-D GRT inversion, see *Bostock et al.* [2001].

[20] The 2-D GRT inversion operates on a series of individual forward- and backscattered modes. The contribution of each mode is inverted based on analytical expressions for the traveltimes and amplitudes of the relevant combination of incident and scattered waves [*Rondenay et al.*, 2001]. In particular, we consider the following scattering modes (see, e.g., *Rondenay et al.* [2010] for the full list of modes): the incident P-wave forward scattered as an S-wave (P_ds); the free-surface-reflected P-wave backscattered as a P-wave (Pp_dp); the free-surface-reflected P-wave backscattered as an S-wave (Pp_ds); and the free-surface-reflected S-wave backscattered as an Sv-wave (Ps_dsl_v) and Sh-wave (Ps_dsl_h). The various scattering modes are weighted based on the rationale developed in *Rondenay et al.* [2001].

[21] The theoretical resolution of the 2D-GRT has been extensively studied using synthetic and field data [*Bostock et al.*, 2001; *Shragge et al.*, 2001; *Rondenay et al.*, 2005, 2008; *Rondenay*, 2009], and has been shown to depend largely on the frequency content of the scattered signal and on the source/receiver distribution. The maximum volume resolution is approximately equivalent to a quarter of the wavelength of the scattered signal (for backscattered waves). Given the high cut-off frequency of 0.5 Hz used in this study, we expect a maximum volume resolution on the order of 2–3 km for structure in the lower crust and upper mantle.

[22] The robustness of the resulting images has been shown to depend largely on the degree to which the geometrical assumption of the technique are met in a given study area [*Rondenay et al.*, 2005]. For the western Hellenic system, given the rapid transition in lithosphere composition and convergence rates between the southern and northern segments, we expect along-strike variations in subsurface structure that may violate the 2-D assumption. The potential effects of these variations on the resulting image will be tested in section 6.2 by examining contributions from events with different back-azimuths.

4. Data

[23] The data analyzed in this study were collected using portable, three-component broadband seismometers from the IRIS-PASSCAL instrument pool. The instruments were deployed in two temporary arrays: a first array spanning across southern Greece was operational from June 2006 to October 2007 (SL); and a second array extending across northern Greece was operational from November 2007 to April 2009 (NL). Each temporary array was deployed roughly perpendicular to the strike of the western Hellenic subduction

Table 1. Optimal 1D Background Velocity Model for SL Imaging[a]

Layer	Z (km)	α (km/s)	β (km/s)	ρ (kg/m³)
1	20	6.2	3.6	2.6
2	40	6.8	3.8	2.8
3	60	7.6	4.2	3.0
4	-	8.0	4.5	3.2

[a]Z is the depth from the free surface to the bottom of the layer, α is P wave velocity, β is S wave velocity, and ρ is density.

zone in a fan-shaped pattern, as shown in Figure 1a. The array geometry was chosen to provide dense station coverage near the trench for maximum resolution at shallow depths and a more diffuse cloud of stations further from the trench to accommodate other types of seismic analyses (e.g., tomography, surface waves dispersion, shear wave splitting).

[24] As in previous applications of 2-D GRT inversion, the selection of useful events is done on the basis of the following criteria [see, e.g., *Rondenay et al.*, 2001, 2005; *Suckale et al.*, 2009]: (1) epicentral distance from the center of the array between 30°–90°, to avoid mantle transition zone triplications and the core shadow zone; (2) a magnitude (Ms, Mb, or Mw) greater than 5.5; (3) an incident P wave arrival that can be identified across the entire array; (4) no overlaps with foreshocks or aftershocks; and (5) minimal contamination of the coda by secondary phases (e.g., PcP, PP). To avoid biases in back-azimuthal coverage that could affect the resulting image, we tighten the selection criteria for regions that are seismically very active and thus return large numbers of events – for example Indonesia. For such regions, we apply the 2-D GRT to each event and include only the events that yield consistent structure across each scattering mode image. The combination of selection criteria and improved preprocessing workflow (c.f., section 3.1) allowed the inclusion of events from regions of sparse and relatively weak seismicity, such as central Africa. As a result, we obtained over 50 high-quality events with comprehensive back-azimuthal distribution for both NL and SL arrays (Figure 1b; Tables S1 and S2 of the auxiliary material).[1]

[25] A last measure of data selection and preprocessing is implemented to account for the fact that stations from both arrays were installed in small buildings such as churches and monasteries, as described by *Suckale et al.* [2009]. This issue is addressed by performing tight quality control on the data to assure the removal of site-specific noise. Specifically, the spectral content of the signal recorded at each station is inspected for every selected event. Based on this information, a unique filter that emphasizes body wave signal is designed and applied to each station-event pair. Station-event pairs that exhibit excessive noise within the body wave band are excluded from the analysis. On average, this procedure leads to the removal of 2 to 4 stations for each event, with no significant loss in sampling density or aperture of the array.

5. A Priori Model Parameters

[26] The 2-D GRT inversion relies on the a priori knowledge of two sets of model parameters: the 2-D regional strike

and the background velocity field. The 2-D regional strike is the dominant azimuth of line-scatterers in the model space. In the case of a subduction zone, it is often considered to be the azimuth perpendicular to the line of the slab's steepest descent [see, e.g., *Rondenay et al.*, 2010]. For a cloud of stations, the 2-D strike may be found by producing images along profiles of various azimuths and determining the azimuth that yields the most focused signal from the subducted crust. This exercise applied to both SL and NL arrays yields an optimal 2-D strike of N30W $\pm$ 10°, meaning that the profiles will be computed along an azimuth of N60E (see Figure S1 of the auxiliary material for details). We note that local estimates of the slab dip-direction along the southern Peloponnesus derived from multiazimuth analysis of receiver functions show counterclockwise deviations from N60E by $\sim$20° [*Gesret et al.*, 2011]. However, these local deviations in dip-direction are unlikely to influence the SL image because the analyzed stations are >50 km to the south of SL (see section 6.2), and show some evidence for a rotation toward N60E from south to north (i.e., toward SL).

[27] An optimal background velocity model is determined by identifying the 1-D P- and S-wave velocity model that produces a consistent location of target structures (e.g., overriding Moho, subducted crust) between different scattering modes. We start with a 1-D P wave model for SL and NL derived by averaging P wave velocities from local tomographic models beneath each line [*Papazachos et al.*, 1995; *Papazachos and Nolet*, 1997]. We then adjust the 1-D S-wave velocities in each model layer using realistic values of Vp/Vs ratios until we obtain a consistent location of the target structures between each scattering mode image (see Figure S2 of the auxiliary material for details). This procedure yields optimal 1-D velocity models for SL and NL that are described in Tables 1 and 2, respectively.

[28] Uncertainty in the appearance of target structures, beyond that related to the theoretical resolution of the 2-D GRT (c.f., section 3), may also be caused by velocity heterogeneity and anisotropy not adequately represented by the optimal background model [*Rondenay et al.*, 2005]. While such uncertainties are difficult to quantify, we can estimate them by applying the 2-D GRT to both real data and synthetic data computed with the RAYSUM package [*Frederiksen and Bostock*, 2000] for a range of realistic Vp/Vs and anisotropic parameters. The results of this test suggest that discontinuities in the composite image have a dip uncertainty of <3° and a depth uncertainty of <4 km, and that a low-velocity layer exhibiting typical velocity reduction for subducted

Table 2. Optimal 1D Background Velocity Model for NL Imaging[a]

Layer	Z (km)	α (km/s)	β (km/s)	ρ (kg/m³)
1	20	6.0	3.4	2.6
2	40	6.8	3.8	2.8
3	60	7.7	4.3	3.0
4	-	8.0	4.5	3.2

[a]Z is the depth from the free surface to the bottom of the layer, α is P wave velocity, β is S wave velocity, and ρ is density.
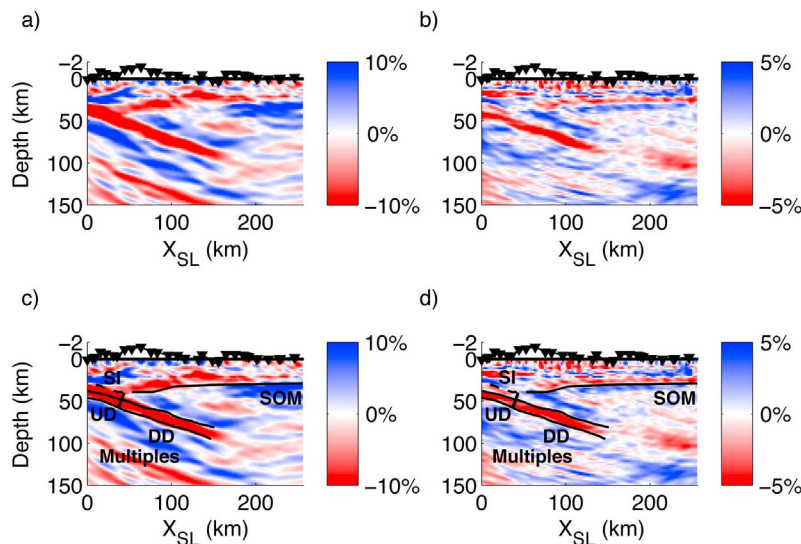
Figure 3. Composite images for SL showing (a, c) $\delta\alpha/\alpha$ and (b, d) $\delta\beta/\beta$ perturbations obtained by 2-D GRT inversion. Figures 3c–3d show the same images as Figures 3a–3b but also include our structural interpretations (black lines): the updip (UD) and downdip (DD) segments of the subducted crust, the location of the thick subduction channel interface (SI), and the Moho of the overriding plate (SOM). Black triangles denote the station locations along SL with 10:1 vertical exaggeration in elevation (i.e., negative depth).

oceanic crust [*Hacker and Abers*, 2004] has a thickness uncertainty of <4 km.

6. Results

[29] In this section, we describe the 2-D GRT images obtained across the southern and northern segments of the western Hellenic subduction zone. First, we show the composite images beneath the SL and the NL arrays, which are produced by simultaneous inversion of all selected events. Then, we present images formed using a subset of events from different back-azimuths to examine along-strike variations in lithospheric structure.

6.1. Composite Images

[30] The composite images for SL and NL are shown in Figures 3 and 5, respectively. They are produced by simultaneously inverting all the events selected for each array (Figure 1b; see Tables S1 and S2 of the auxiliary material), using the profile orientations shown in Figure 1a and the background velocity models from Tables 1 and 2. The images show perturbations in either P- or S-wave velocity with red representing a velocity reduction and blue a velocity increase. The method is sensitive to velocity discontinuities, which are identified by crossovers in the color scale, i.e., red-to-blue indicating slow-to-fast and blue-to-red indicating fast-to-slow velocity perturbations. In the remainder of this paper, we will refer to discontinuities marking an increase/ decrease in velocity with depth as positive/negative discontinuities, respectively.

[31] As in previous applications of the 2-D GRT, we will focus our discussion on the S-velocity ($\delta\beta/\beta$) profile, as $\delta\beta/\beta$ images have been shown to be more robust than the $\delta\alpha/\alpha$ images [*Rondenay et al.*, 2001, 2005; *Rondenay*, 2009]. However, the $\delta\alpha/\alpha$ profiles are also shown as they help

support the identification of actual structures as opposed to artifacts from multiples, which are more prevalent in the $\delta\beta/\beta$ images.
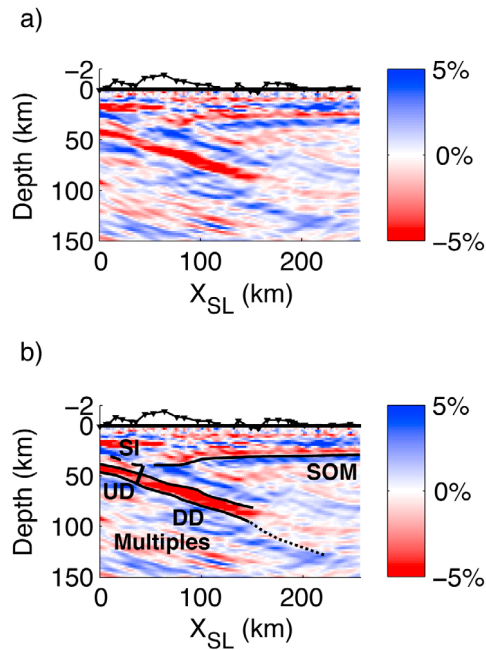
6.1.1. SL Composite Image

[32] The SL composite images show two prominent features: a low velocity layer (LVL) dipping to the ENE from ~30 to 80 km depth, and a positive, sub-horizontal discontinuity with an average depth of ~35 km (Figure 3). These structures are similar to those found by *Suckale et al.* [2009]; however, the improved resolution in this study allows us to clarify several issues raised in that paper.

[33] The LVL dips at ~17° with an average thickness of ~8 km (Figure 3), which is significantly thinner than the 15–20 km thickness reported in *Suckale et al.* [2009]. It appears to change thickness abruptly at a depth of ~40 km, leading us to separate it into updip and downdip segments. The updip segment (i.e., above 40 km depth) is characterized by a greater average thickness of ~12 km, a sharp upper boundary, and some potential internal structure. Conversely, the downdip segment (i.e., below 40 km depth) thickens gradually from 7 km to 10 km with increasing depth and is marked by a more diffuse upper boundary. The $\delta\beta/\beta$ magnitudes along the top and bottom of the LVL are approximately −10% and +10%, respectively. However, the magnitude of these perturbations should be interpreted with caution because of 1) the rather diffuse color crossovers marking the upper and lower boundaries of the LVL, and 2) the potential for amplification effects due to data sparseness – an effect that has been documented in numerical and field data examples [*Rondenay et al.*, 2005; *MacKenzie et al.*, 2010].

[34] The signal marking the top of the LVL diminishes rather abruptly at a depth of ~80 km on both the $\delta\alpha/\alpha$ and $\delta\beta/\beta$ composite images, while a faint signal from the base of the LVL appears to continue to ~125 km depth. We can

a)

b)

Figure 4. (a) Composite images for SL showing $\delta\beta/\beta$ obtained by 2-D GRT inversion of free-surface-reflected phases only (i.e., Pp_dS, $Ps_dS|_v$, and $Ps_dS|_h$). (b) The same image as Figure 4a but also includes the structural interpretations from Figures 3c and 3d plus the extension of the subducted Moho to ~125 km depth (dotted line). Black triangles denote the station locations along SL with 10:1 vertical exaggeration in elevation (i.e., negative depth).

assess the robustness of the signal marking the base of the LVL between 80 and 125 km by considering the contributions of the individual scattering modes to the final image (Figure S2a of the auxiliary material). As was already noted in the study of *Suckale et al.* [2009], this signal is strong on all the individual modes but it does not necessarily stack constructively because of LVL dip discrepancies between the forward and backscattered modes (see Figure S2 and discussion in the auxiliary material). We note that when the image is constructed using only the backscattered modes (Figure 4), the base of the LVL produces a strong and robust signal down to 125 km depth.

[35] The positive sub-horizontal discontinuity emerges from near the separation between the updip and downdip segments of the LVL (Figure 3) and is clearly observed at ~40 km depth beneath the Hellenides (X_{SL} = 60 km). It shallows rapidly to ~34 km beneath the eastern Peloponnesus (X_{SL} = 150 km) then dips gently beneath eastern Greece to attain a depth of ~30 km beneath the Aegean coast (X_{SL} = 250 km). The discontinuity exhibits an average $\delta\beta/\beta$ of approximately +10% beneath the Hellenides and eastern Greece. Its magnitude is more difficult to estimate in the region adjacent to the LVL and beneath the eastern Peloponnesus. The interpretation and implications of these observations are discussed in section 7.1 and 7.3.

6.1.2. NL Images

[36] The NL composite images show two features similar to those observed to the south: a low velocity layer (LVL) dipping to the ENE from ~30 to 70 km depth and a positive, sub-horizontal discontinuity with an average depth of 40 km (Figure 5).

[37] The LVL dips at approximately 17° and has an apparent thickness that increases from 12 km to 20 km with increasing depth (Figure 5). The base of the LVL is continuous and clearly identified down to a depth of nearly 100 km,

a)   b)

c)   d)
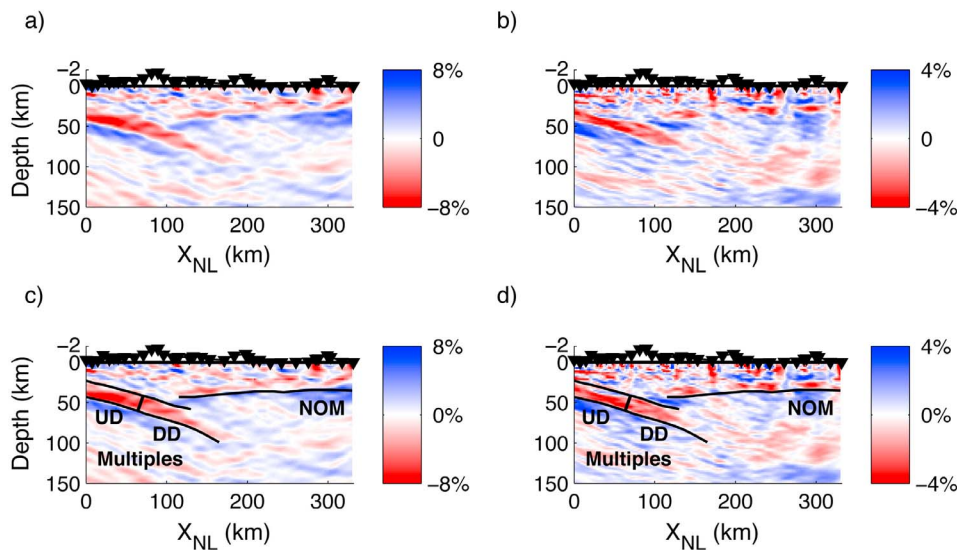
Figure 5. Composite images for NL showing (a, c) $\delta\alpha/\alpha$ and (b, d) $\delta\beta/\beta$ perturbations obtained by 2-D GRT inversion. Figures 5c–5d show the same images as Figures 5a–5b but also include our structural interpretations (black lines): the updip (UD) and downdip (DD) segments of the subducted crust, and the Moho of the overriding plate (NOM). Black triangles denote the station locations along NL with 10:1 vertical exaggeration in elevation (i.e., negative depth).
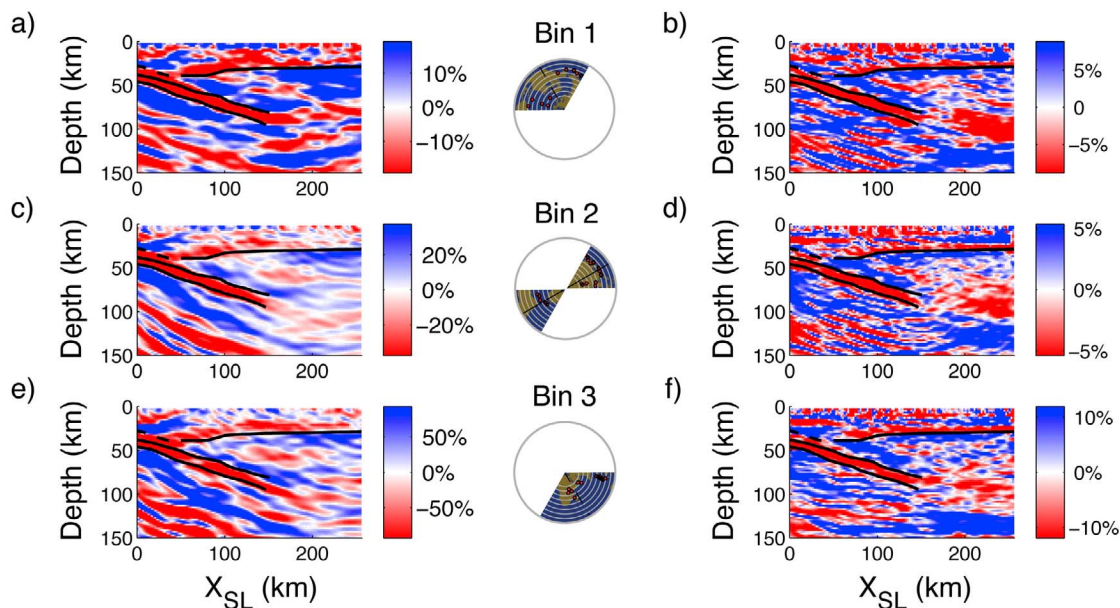
Figure 6. SL images of $\delta\alpha/\alpha$ (Figures 6a, 6c, 6e) and $\delta\beta/\beta$ (Figures 6b, 6d, 6f) perturbations obtained for subsets of the data divided into back-azimuthal bins: (a, b) bin 1 uses events from NNW, (c, d) bin 2 uses events from WSW and ENE, and (e, f) bin 3 uses events from SSE. Interpreted structural boundaries (black lines) are the same as in Figure 3. The color scale varies between panels to take into account variations in the number and the quality of events used to generate each image, something that can cause significant amplitude variations when illumination is incomplete [see *Rondenay et al.*, 2005].

with a consistent location in both the $\delta\alpha/\alpha$ and $\delta\beta/\beta$ images. It exhibits an average $\delta\beta/\beta$ of +7% marked by a progressive reduction in magnitude with increasing depth. Conversely, the top boundary of the LVL exhibits different signatures updip and downdip of ~50 km depth, leading us to separate it into two segments as was done for SL. The updip segment (i.e., above 50 km depth) comprises a thinner basal LVL (~12 km) overlain by several closely spaced discontinuities of limited lateral extent, including a positive discontinuity just above the basal LVL. This complex signature makes it difficult to estimate a meaningful $\delta\beta/\beta$ magnitude. The downdip segment, on the other hand, has a clear negative discontinuity that marks the top of the LVL on both the $\delta\alpha/\alpha$ and $\delta\beta/\beta$ images with a $\delta\beta/\beta$ of approximately −7%. Thus, the downdip segment comprises a single 20 km-thick LVL that disappears between 70 and 90 km depth, in a more gradual fashion than its southern counterpart.

[38] The NL composite images also show a sub-horizontal positive discontinuity that extends across the eastern part of the profile (Figure 5). It appears at a depth of 44 km near the LVL ($X_{NL} \sim 100$ km) and shallows gradually to a depth of 35 km at the eastern edge of NL. The positive discontinuity exhibits large lateral variations in $\delta\beta/\beta$, with three regions having magnitudes averaging +7% centered at X_{NL} = 130, 230 and 280 km separated by two regions that lack signal at X_{NL} = 180 km and X_{NL} = 260 km. The interpretation and implications of these observations are discussed in section 7.2 and 7.3.

6.2. Along-Strike Variations

[39] Along-strike variations in the subduction system beneath NL and SL are investigated by generating images with events from separate back-azimuthal bins, as shown in Figures 6 and 7. Each back-azimuthal bin contains a significant number of events (>14) that illuminate the subsurface from both updip and downdip directions. The different back-azimuthal contributions allow us to isolate scattered waves coming from the north of the profile (bin 1), from below the profile (bin 2), and from the south of the profile (bin 3). In general, obliquely incident waves such as those used in bins 1 and 3 strike the imaging target at a perpendicular offset from the station array, and this offset becomes larger with increasing target depth [*Rondenay et al.*, 2005, 2010]. From the results of *Rondenay et al.* [2005, Figure 5], the maximum perpendicular offset of scattered waves contributing to the bin 1 and bin 3 images is approximately 20 km for targets at 30 km depth, and 40 km for targets at 80 km depth. Thus, bin-specific images provide a means of detecting along-strike variations in the imaging target and testing how well the geometric assumption of the 2-D GRT are met.

[40] Figure 6 shows the SL bin-specific images for $\delta\alpha/\alpha$ and $\delta\beta/\beta$. The thickness and position of the SL LVL are remarkably consistent in both images. We also note that in each bin-specific $\delta\beta/\beta$ image, the LVL exhibits the same updip and downdip attributes as those observed in the composite image (e.g., a thicker layer in the updip segment, see section 6.1.1 and Figure 3). Close examination of the $\delta\alpha/\alpha$ bin-specific image reveals a secondary LVL beneath the primary LVL described in section 7.1.1, which increases in amplitude from the NNW to the SSE (i.e., from bin 1 to bin 3). This feature may be an artifact due to cross-mode contamination, or may be related to along-strike variations in the subduction system, something we discuss further in section 7.3.
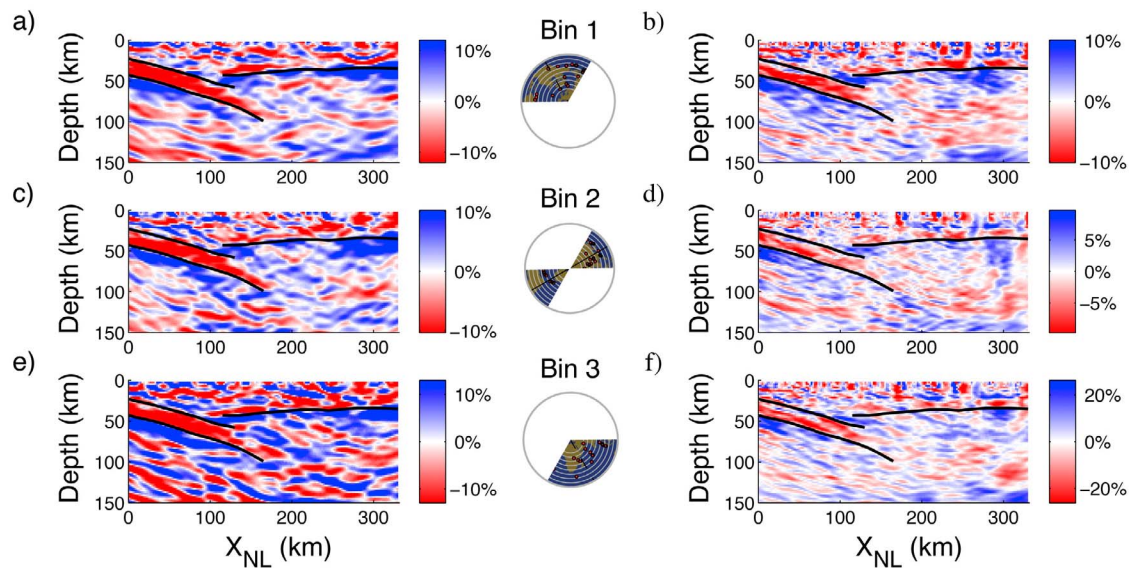
Figure 7. NL images of $\delta\alpha/\alpha$ (Figures 7a, 7c, 7e) and $\delta\beta/\beta$ (Figures 7b, 7d, 7f) perturbations obtained for subsets of the data divided into back-azimuthal bins: (a, b) bin 1 uses events from NNW, (c, d) bin 2 uses events from WSW and ENE, and (e, f) bin 3 uses events from SSE. Interpreted structural boundaries (black lines) are the same as in Figure 5. Note that the velocity perturbations are amplified due to the limited illumination afforded by the subsets of data, but that the structures are still adequately resolved (see *Rondenay et al.* [2005] for a complete discussion of these effects).

[41] Figure 7 shows the NL bin-specific images of $\delta\alpha/\alpha$ and $\delta\beta/\beta$. All of these bin-specific images show an updip segment of the LVL that is remarkably consistent with the composite image in Figure 5. The transition from updip to downdip segments is observed in each bin-specific $\delta\beta/\beta$ image at a depth of ~50 km. However, the seismic signature of the downdip segment varies significantly along strike with a "braided" texture in the bin 3 image compared to the bin 1 and bin 2 images. Along strike variations in the structure of the downdip segment explain its weaker amplitude in the composite image and may be indicative of anisotropy within the downdip segment, something that we discuss further in section 7.2.

7. Discussion

[42] In this section, we discuss the tectonic and geodynamic implications of our seismic images by focusing on three main topics: the southern segment, the northern segment, and the slab structure between these two domains. To aid the discussion, the composite images have been reproduced in Figure 8, along with profiles of local seismicity within 25 km of each line.

7.1. Southern Segment
7.1.1. Nature of the Subducted Slab

[43] The SL composite image shows an ~8 km thick LVL with a dip of ~17° extending into the upper mantle below southern Greece (Figures 3 and 8b). To the west of our profile, marine seismic data have shown that the oceanic crust beneath the abyssal plain of the Ionian Sea consists of 5–8 km of igneous crust [*de Voogd et al.*, 1992; *Finetti and Del Ben*, 2005] overlain by 4–6 km of sediments [*Kopf et al.*, 2003; *Finetti and Del Ben*, 2005]. The similarity in thickness

between the LVL and the igneous crust entering the trench strongly suggests that the LVL represents the continuation of this subducted crust at depth, provided that most of the sediments are scraped off before the crust reaches the mantle wedge. Thus, the subducted lithosphere imaged beneath the southern segment appears oceanic in nature. This interpretation is in agreement with recent receiver function studies that observe a 7 km-thick LVL with a ~17° dip angle at 60 km depth beneath the southern Peloponnesus [*Gesret et al.*, 2010, 2011].

7.1.2. Extent and Duration of Subduction

[44] Based on the total length of the imaged subducted crust and a trench location ~100 km to the west of the profile, we estimate that at least 250 km of oceanic lithosphere has subducted beneath the southern segment (Figure 3). If we assume that the subduction rate along the southern segment has remained constant at the current rate of ~35 mm/yr, the deepest subducted crust beneath southern Greece would have entered the trench ~7 Ma ago. On the other hand, if we consider a gradual increase in subduction rate from 5 to 12 mm/yr during the middle Miocene to 35 mm/yr at present time, as suggested by *Royden and Papanikolaou* [2011], the deepest subducted crust would have entered the trench ~10 Ma ago. These time constraints are consistent with the proposed age of transition from continental to oceanic subduction along the trench of the southern segment [*Royden and Papanikolaou*, 2011] and suggest this transition may currently be located near the termination of the SL subducted crust at depth (see section 7.3 for further discussion of the ocean-continent transition).

7.1.3. Subduction Interface

[45] As first noted in section 6.1, the seismic properties of the subduction interface vary abruptly at a depth of ~40 km, corresponding approximately to its intersection with the
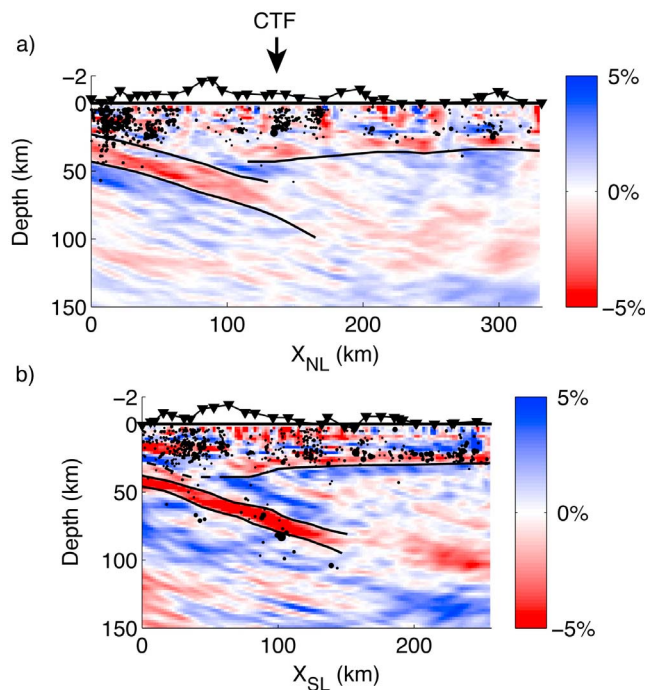
Figure 8. Comparison between the composite $\delta\beta/\beta$ images for (a) NL and (b) SL, with local seismicity within 25 km of each line. Local event hypocenters (black dots) are from the National Observatory of Athens Bulletin. We plot events that occurred from June 2002 to January 2012 and had the following specifications: (1) $M_L \geq 3$, (2) located using time picks from at least 8 stations, and (3) located by groups of stations with an azimuthal separation <150°. Dot size is proportional to magnitude, with the smallest dots corresponding to $M_L = 3$ and the largest dots to $M_L = 5.1$. The black arrow above a) shows where the extension of the Cephalonia transform fault (CTF) intersects NL, as depicted in Figure 10.

overriding Moho. The updip segment appears to comprise closely spaced discontinuities that run near, and parallel to, the subduction interface, producing a thicker LVL (~12 km) than in the lower segment (see region labeled SI in Figure 3). This internal layering may be interpreted in one of two ways. (1) The top boundary represents an inverted Moho resulting from serpentinization of an overriding sliver of mantle wedge, as was suggested to explain receiver functions in this region by *Sodoudi et al.* [2006]. (2) The top layer represents a sediment-filled subduction channel separating overlying forearc crust from the subducted oceanic crust. In both these cases, the lower, positive internal boundary would mark the top of the actual subducted crust as illustrated in Figure 3. The first option is unlikely given that gravity data [*Royden*, 1993; *Tsokas and Hansen*, 1997] and seismic velocities [*Papazachos and Nolet*, 1997; *Karagianni and Papazachos*, 2007] show no evidence for mantle rocks extending in this region beneath the western Hellenides (see *Suckale et al.* [2009] for further discussion). The presence of subduction channel sediments is thus the preferred explanation, as it can explain both the observed negative discontinuity at the top of the subducted crust and the sudden change in LVL thickness at ~40 km depth. The imaged velocity contrast (>10%) is

consistent with a transition from forearc crust above to subducted sediments below, with a potential contribution from high pore fluid pressure, as has been recently suggested for the Cascadia subduction zone [*Abers et al.*, 2009; *Audet et al.*, 2009]. The sudden change in thickness can be explained by the accretion of some of these sediments underneath the overriding crust [see, e.g., *Waschbusch and Beaumont*, 1996; *Ellis et al.*, 1999; *Beaumont et al.*, 1999], a process that would be confined to depths shallower than that of the overriding Moho, and/or by a sudden drop in fluid pressures as the subduction interface transitions from overriding crust into the mantle wedge [see, e.g., *Audet et al.*, 2009]. The downdip segment (50–80 km depth) is marked by a single, negative discontinuity yielding an LVL thickness of 8 to 10 km. The region above the downdip segment has been shown to have relatively low attenuation and heat flow [*Hashida et al.*, 1988; *Fytikas and Kolios*, 1979]. Based on a comparison with thermal models, these geophysical observations suggest that a relatively cold (i.e., stagnant) portion of the mantle wedge overlies the segment of the subduction interface extending from 50 to 80 km [*Wada and Wang*, 2009; *Syracuse et al.*, 2010].

7.1.4. Disappearance of the Subducted Crust at Depth

[46] As observed in Figure 3 (see also Figure S2 of the auxiliary material), the seismic signal marking the top of the subducted crust disappears abruptly at approximately 80 km depth, while a faint signal attributable to the subducted Moho remains visible to depths of ~125 km. The loss of signal from the top boundary is attributed to widespread dehydration of the upper crust's basaltic layer as it undergoes eclogitization, as has been documented in numerous subduction zones using similar imaging techniques [*Rondenay et al.*, 2008; *Abers et al.*, 2009; *MacKenzie et al.*, 2010]. A rapid increase in attenuation, conductivity, and heat flow has also been observed above where the top of the subducted crust disappears [*Hashida et al.*, 1988; *Fytikas and Kolios*, 1979; *Galanopoulos et al.*, 2005], which suggests this region sits within the circulating portion of the mantle wedge [*Wada and Wang*, 2009; *Syracuse et al.*, 2010]. Thermal and petrologic modeling by *van Keken et al.* [2011] also predicts the rapid dehydration of the Ionian slab's upper crust at ~80 km depth while the lower gabbroic crust and upper slab mantle remain hydrated to significantly greater depths (>200 km). This latter prediction explains why the signal of the subducted Moho may persist (albeit faintly) down to at least 125 km depth.

7.1.5. Moho of the Overriding Plate

[47] The positive, sub-horizontal discontinuity imaged in our SL profile at ~35 km depth is interpreted as the Moho of the overriding plate (Figure 3). It exhibits depth fluctuations that are broadly consistent with isostatic compensation of surface topography, in agreement with prior results obtained by *Suckale et al.* [2009]. Thus, we refer the reader to that paper for a detailed discussion of the structure of the overriding plate.

7.2. Northern Segment

7.2.1. Nature of the Subducted Slab

[48] The NL composite image shows a ~20 km thick LVL dipping at ~17° within the upper mantle beneath northern Greece (Figures 5 and 8a). Marine seismic data have shown that the continental crust within the foreland consists of ~20 km of crystalline crust overlain by ~8 km of sediments

[Finetti and Del Ben, 2005]. The LVL is thus interpreted as subducted continental crust, provided that ∼8 km of sediments are being scraped from the subducting slab and accreted into the thrust belt of the overriding plate. Our interpretation is in agreement with recent geodynamic models of continental subduction along the northern segment, which suggest that ∼10 km of crustal material must be removed from the continental lithosphere in order to achieve a buoyancy that is sufficiently negative to match present-day subduction rates of 5–8 mm/yr [Royden and Papanikolaou, 2011].

7.2.2. Extent and Duration of Subduction

[49] Based on the imaged extent of the subducted continental crust (Figure 5) and the trench location ∼50 km seaward of the NL line [Moretti and Royden, 1988; Finetti and Del Ben, 2005], we estimate that at least 220 km of continental lithosphere has subducted beneath the northern segment. Royden and Papanikolaou [2011] provide bounds on the subduction rates along northern Greece since Late Eocene to be 5–8 mm/yr from 0 to 5 Ma ago, 5–12 mm/yr from 5 to 20 Ma ago, and 25–35 mm/yr from 20 to 35 Ma ago. From these estimates, the deepest subducted continental crust would have entered the trench between 20 and 25 Ma ago. This analysis suggests continuous subduction of continental lithosphere along the northern segment since the early Miocene, in general agreement with the record of subduction inferred from the nappes of the external Hellenides along NW Greece [van Hinsbergen et al., 2005; Papanikolaou, 2009].

7.2.3. Subduction Interface

[50] Having made the case for continental subduction along the northern segment, we now look more closely at the structure of the plate interface. First, we examine the updip segment of the subducted crust, which comprises a ∼12 km thick LVL overlain by several closely spaced discontinuities (Figure 5). Local tomographic models show that the region above the subducted continental crust observed in the $\delta\beta/\beta$ image (Figure 5) has relatively low P- and S-velocities consistent with accreted sediments [Papazachos and Nolet, 1997]. In this case, the subduction interface would not manifest itself as a negative discontinuity (as was interpreted for SL) but instead would be marked by a positive discontinuity resulting from the velocity contrast between the sediments accreted to the overriding plate (above) and the crystalline crust of the subducting continental slab (below). Thus, we interpret the positive discontinuity above the ∼12 km thick LVL (upper solid black line in the UD segment of Figure 5) as the top of the subducted crystalline crust, an interpretation consistent with both the thickness and position of the crystalline crust observed in marine seismic data (see sections 7.2.1 and Figure 9). The closely spaced discontinuities above the top of the subducted crust appear to be of limited lateral extent and may reflect internal structure within a broad subduction channel in which subducted sediments, and perhaps some crystalline crust, are being detached from the slab and accreted to the overriding plate. Such broad subduction channels are predicted by thermal-mechanical models of retreating continental subduction boundaries [e.g., Warren et al., 2008] and may favor the subduction of the entire crystalline crust into the mantle [De Franco et al., 2008].

[51] The subduction interface of the downdip segment is clearly marked by a single negative discontinuity, which we attribute to the transition from mantle peridotites (above) to crystalline continental crust (below). We note, however, that the velocity contrast observed is weaker than that expected for a peridotite to continental crust transition [Hacker et al., 2003; Hacker, 2008]. This is due, at least in part, to the along-strike variations of the NL subducted crust discussed in section 6.2 (Figure 7), which leads to the defocusing of the crust [Rondenay et al., 2005].

7.2.4. Disappearance of the Subducted Crust at Depth

[52] The seismic signal from the top of the subducted crust disappears at a depth of ∼70 km, while the subducted Moho persists to a depth of nearly 100 km. There are several possible explanations for the loss of seismic signal from the subducted crust. First, it may be partially due to a loss in image resolution in this depth range. Indeed, multiples from the continental Moho appear to contaminate the $\delta\alpha/\alpha$ and $\delta\beta/\beta$ images at ∼100 km and ∼80 km, respectively (Figure 5). In addition, the dip of the subducting continental slab may increase rapidly within this depth range due its slower rate of rollback, as has been suggested by geodynamic models [Royden and Husson, 2006, 2009]. This could cause the lower part of the slab to dip too steeply to be resolved by the 2-D GRT [see, e.g., Rondenay et al., 2005; MacKenzie et al., 2010]. Second, the subducted crust may undergo progressive dehydration via eclogitization, as has been suggested for oceanic subduction zones [e.g., Rondenay et al., 2008]. Progressive dehydration of subducting continental lower crust has also been interpreted beneath the northern Apennines based on receiver function images of an anisotropic, low S-velocity layer at 45–65 km depth [Agostinetti et al., 2011]. Furthermore, thermal-mechanical models predict a similar conversion of continental lower, and possibly middle, crust to eclogite and/or coesite eclogite [Warren et al., 2008], which have seismic velocities similar to those of mantle peridotites and could thus explain the loss of seismic signal [Hacker and Abers, 2004]. If slab dehydration is occurring along the downdip segment, it appears to do so without generating intermediate depth earthquakes (Figure 8a), unlike oceanic subduction settings where such earthquakes are commonly attributed to dehydration reactions [Hacker et al., 2003]. Third, the termination of the downdip segment could be the result of a slab tear – something we discuss in section 7.3.

7.2.5. Moho of the Overriding Plate

[53] The positive, sub-horizontal discontinuity imaged in our NL profile at ∼40 km depth is interpreted as the Moho of the overriding plate (Figure 5). It gradually shallows from the eastern edge of the Hellenides to the northern Aegean, in qualitative agreement with previous studies [Marone et al., 2003; Sodoudi et al., 2006]. However, the high-density array used in this study reveals details of its structure that exceed the resolution of previous studies. The strength of its signal varies greatly as a function of location, with three distinct high-amplitude regions separated by two regions where no clear Moho signal exists. These variations may be related to the complex tectonic evolution of northern Greece, which has experienced the subduction and accretion of alternating continental fragments and oceanic basins [van Hinsbergen et al., 2005; Papanikolaou, 2009].
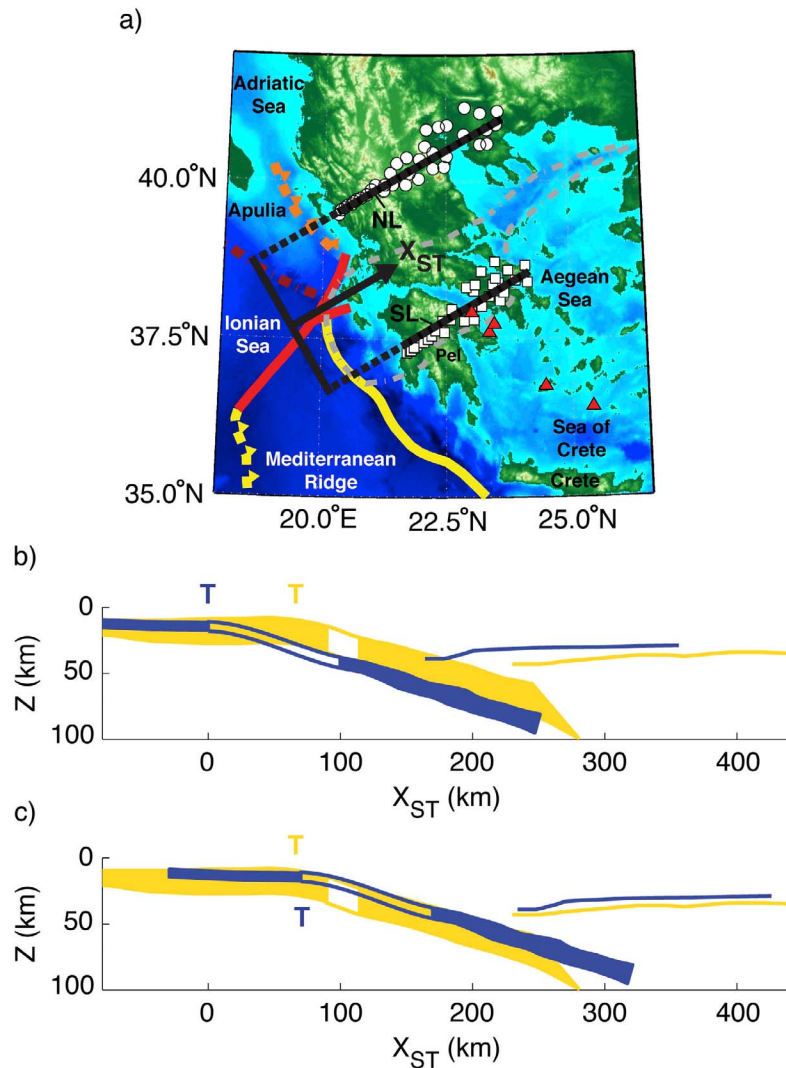
Figure 9. Comparison between the northern and southern slab geometry. (a) Map showing the common coordinate system (X_{ST}) used to compare the NL and SL slab geometries, which is oriented along the optimal projection lines of NL and SL (N60E, see black arrow) and has its origin at the intersection of SL and the southern trench (solid black line at $X_{ST} = 0$). (b) Relative positions of the NL (gold) and SL (purple) subducted crusts and overriding Mohos imaged in this study (solid), with connection to the approximate location of the foreland crust inferred from surface seismic studies (beneath the unconnected black squares in Figure 9a) [*Finetti and Del Ben*, 2005]. Unfilled subducted crust regions show interpolation between two imaged structures. Also shown are the approximate trench locations along SL (purple T) and NL (yellow T). (c) Same as Figure 9b, but with a landward horizontal displacement of 70 km (i.e., to the right, as shown by the translation of the purple T) applied to the SL slab and overriding crust. Note that the *x* axis in Figure 9c does not have geographical significance as we have not accounted for the absolute motion of the northern segment.

7.3. Slab Geometry Along the WHSZ

[54] Understanding the variations in slab geometry from the northern to the southern seismic profile can yield important insight into how a single subduction system accommodates a transition from continental to oceanic slab subduction. Figure 9 shows an along-strike view of the mantle wedge along the WHSZ constructed based on the interpreted structures from Figures 3 and 5, along with the foreland crustal structure inferred from marine seismic data [*Finetti et al.*, 1991; *Finetti and Del Ben*, 2005]. The outlines depicted in Figure 9b exhibit two interesting features: 1) the oceanic subducted crust beneath SL appears to sit deeper than the continental subducted crust beneath NL, and 2) the portions of the slab beneath NL and SL have similar dips despite their differences in crustal thickness. In the following, we discuss the implications of these observations as they relate to differential slab retreat, the flexural strength of the slab, and the connection between the two imaged portions of the slab.
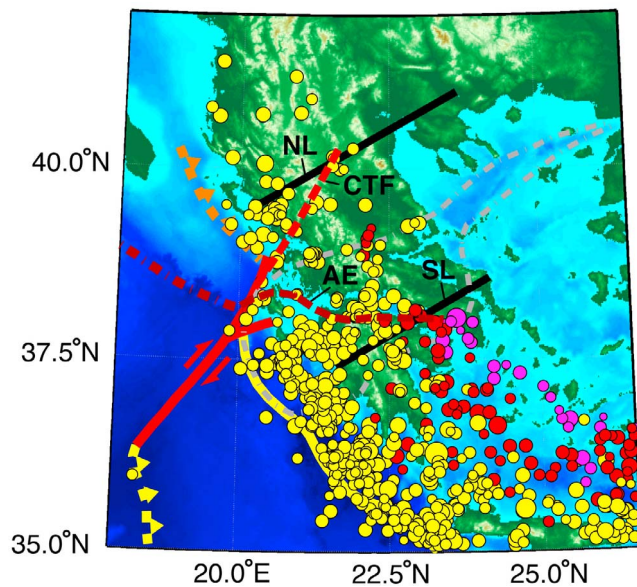
Figure 10. Map of Greece showing the location of deep seismicity (>50 km) from the International Seismological Centre (http://www.isc.ac.uk) catalog with reported depth errors less than 10 km. We map events that occurred between January 1964 to May 2006, using the following color code for hypocenter depth: 50 km–100 km (yellow), 100 km–150 km (red), and >150 km (purple). The two potential tear locations discussed in the text are also shown: (1) the approximate location of the Apulian escarpment (AE, ocean-continent transition) beneath southern Greece, as estimated from the paleogeographic reconstruction of *Royden and Papanikolaou* [2011], is denoted by a dashed brown line, and (2) the Cephalonia transform fault (CTF) beneath northern Greece is denoted by a dashed red line. The surface projection of our two 2D-GRT profiles are denoted by thick black lines (SL and NL).

7.3.1. Differential Slab Retreat Between the Northern and Southern Portions of the Slab

[55] The geometrical attributes of the WHSZ, as depicted in Figure 9b, bear remarkable resemblance to the simple model of differential retreat shown in Figure 2. To explore this link further, quantitative estimates of differential retreat are derived from Figure 9b and compared to the offset of the WHSZ produced by the Cephalonia transform fault. We have to make some simplifying assumptions to do this analysis, namely that the trench of the WHSZ was originally linear and that the slab maintained a constant dip at depths <100 km after it segmented. These assumptions are reasonable given that (1) geologic and GPS observations suggest recent (latest Miocene to Pliocene time) segmentation of a previously continuous thrust belt that extended along the WHSZ [*Reilinger et al.*, 2010; *Royden and Papanikolaou*, 2011]; and (2) our images show that the two slab segments currently have similar dips despite their differences in crustal thickness (see section 7.3.2). Using the subducted crust outlines in Figure 9b, we calculate an additional 70–85 km of seaward retreat for the southern portion of the slab compared to the northern portion (see auxiliary material for further details). This estimate of differential retreat is similar to the ~100 km offset produced by the Cephalonia transform fault. Thus our

seismic images provide evidence in support of segmentation of the WHSZ through differential slab retreat.

7.3.2. Similar Geometries for the Northern and Southern Portions of the Slab?

[56] The dip of the slab at shallow depths (~30 to 100 km) is remarkably similar beneath the northern and southern portions of the WHSZ (Figure 9c), despite their differences in crustal thickness and buoyancy. Such lack of correlation between slab dip and buoyancy has also been observed in global compilations of oceanic subduction zone attributes [e.g., *Lallemand et al.*, 2005; *Cruciani et al.*, 2005]. A variety of mechanisms have been invoked to explain shallow slab dip including flow associated with plate motions [*Hager and O'Connell*, 1978]. *Lallemand et al.* [2005] find that slab dip at shallow depths is globally correlated with the rates of absolute motion of the subducting plate, the trench, and the overriding plate. However, the WHSZ does not show a correlation of these factors with slab dip; the trench and overriding plate motions vary greatly between the northern and southern slab segments, while the shallow slab dip is uniform.

[57] Other factors that may affect slab dip include buoyancy and flexural slab strength (see subduction dynamics review by *Becker and Faccenna* [2009] for discussion of processes affecting slab dip and references). *Royden and Husson* [2006] developed a dynamically consistent subduction model that accounts for a wide variety of subduction processes with boundary conditions appropriate for the WHSZ (see discussion in *Royden and Papanikolaou* [2011]). Their models show that slab buoyancy strongly influences trench retreat rates but does not greatly influence shallow slab dip. They show instead that several other factors may play a prominent role in determining slab dip at shallow depths. These include the flexural slab strength (elastic or viscous) and the thickness and density of the overriding plate and accretionary prism.

[58] While a detailed analysis of these factors is beyond the scope of this paper, there is independent evidence that the slab's flexural strength may be an important factor [*Moretti and Royden*, 1988; *Royden*, 1993]. Gravity and flexure data yield an elastic thickness estimate for the southern segment of 70 km [*Royden*, 1993] and a lower limit of 20 km for the northern segment, with larger values permissible provided that flexure-inducing loads are correspondingly increased [*Moretti and Royden*, 1988]. *Royden and Husson* [2006] show that slabs with elastic thicknesses greater than ~30 km have shallow dips (<~20°) persisting to at least 70–80 km depth, similar to what is seen in our images (Figure 9c). Moreover, variations in elastic thicknesses over 30 km do not greatly affect the retreat rate, which is instead dominated by slab buoyancy and other factors cited above [see *Royden and Husson*, 2006, Figure 10]. Thus, we propose that the two portions of the WHSZ slab have different retreat rates resulting primarily from their different buoyancies, while they exhibit similar low dips at shallow depths because their flexural rigidities are similar and large (i.e., ~70 km). If this inference is correct, it supports the assumption of constant slab dip over time.

7.3.3. Transition From the Northern to the Southern Portion of the Slab

[59] We now turn out attention to the possible links between the northern and southern segments. First we

consider the case of a smooth, continuous ramp between the two segments. The trench-parallel distance between the NL and SL profiles is ~270 km and the vertical offset between the Moho of the subducted crusts within the upper mantle is ~10 km (Figure 9). Accordingly, a smooth ramp between the Moho of the NL and SL subducted crusts would require a slope of only ~2° dipping to the SSE. Such a model is consistent with the following constraints from previous investigations: 1) the presence of a continuous, high-Q slab between NL and SL [*Konstantinou and Melis*, 2008]; 2) the continuity of the high-velocity anomaly in local tomographic models beneath central Greece [*Papazachos and Nolet*, 1997]; 3) the continuity of the slab Moho in the S receiver functions of *Sodoudi et al.* [2006] (albeit at much greater depth beneath northern Greece than our NL image); and 4) the slab depth of ~75 km beneath the western Gulf of Corinth inferred by *Zelt et al.* [2005].

[60] Second, we explore the possibility that the northern and southern portions of the slab are separated by a tear. We consider the two possible tear locations that have been proposed in the literature (see section 1): along the Cephalonia transform or along the ocean-continent transition. The Cephalonia transform is a possible candidate because its extrapolation into northern Greece intersects the downdip segment of the NL subducted crust at a depth of ~70 km, very close to where the low-velocity signal of the subducted crust disappears (70–100 km depth; compare Figures 8 and 10). A tear along the ocean-continent transition is more difficult to reconcile with our seismic images. Indeed, while this structure intersects the SL subducted crust at ~80 km, a signal attributable to the subducted Moho is observed well beyond that depth, which would argue against tearing of the slab in this region.

[61] To summarize, the simplest (and arguably best supported) form of transition between the northern and southern portions of the slab is a smooth ramp – at least for the top ~100 km of the system. Nevertheless, a slab tear along the Cephalonia transform fault cannot be ruled out, though the disappearance of the subducted crust at ~70–100 km depth can be equally explained by eclogitization reactions (see section 7.2.4). Future studies using additional imaging techniques (e.g., receiver functions, local tomography, etc.) and data from trench/arc-parallel receiver arrays [e.g., 'THALES WAS RIGHT', Sachpazi *et al.*, in prep.] should provide a more detailed picture of the connection between the two segments.

8. Concluding Remarks

[62] In this study, a 2-D GRT migration algorithm was applied to teleseismic data collected by two arrays of broadband seismographs to generate high-resolution seismic images across the northern and southern segments of the western Hellenic subduction zone. These images were used to draw the following conclusions regarding the structure and dynamics of a system that involves a transition from oceanic to continental subduction:

[63] 1. Subducted crust is observed beneath both the northern and southern segments of the WHSZ (Figures 3 and 5, respectively) and both segments have a similar strike of approximately N30W +/− 10° and dip of approximately 17°.

[64] 2. The ~8 km thick subducted crust beneath the southern segment is interpreted as the oceanic crust of the Ionian (Sea) lithosphere, provided that most of the overlying sediments are scraped off before the crust reaches the mantle wedge.

[65] 3. The ~20 km thick subducted crust beneath the northern segment is interpreted as the crystalline continental crust of the Apulian lithosphere, which has a thickness and position consistent with constraints on the foreland continental crust from marine seismic data, provided that ~10 km of overlying sediments have been accreted to the overriding plate.

[66] 4. The offset between the SL and NL subducted crusts implies 70–85 km of additional slab retreat along the southern segment as compared to the northern segment, which is in general agreement with the offset of ~100 km along the Cephalonia transform fault.

[67] 5. A smooth ramp between the two slab segments is the simplest model for their connection in the top ~100 km of the system, as it only requires an arc-parallel slope of approximately 2°. Nevertheless, based on our 2-D profiles we cannot rule out a slab tear along the Cephalonia transform fault or (for depths >100 km) the ocean-continent transition.

References

Abers, G. A., L. S. MacKenzie, S. Rondenay, Z. Zhang, A. G. Wech, and K. C. Creager (2009), Imaging the source region of Cascadia tremor and intermediate-depth earthquakes, *Geology*, *37*(12), 1119–1122, doi:10.1130/G30143A.1.

Agostinetti, N. P., I. Bianchi, A. Amato, and C. Chiarabba (2011), Fluid migration in continental subduction: The northern Apennines case study, *Earth Planet. Sci. Lett.*, *302*, 267–278, doi:10.1016/j.epsl.2010.10.039.

Armijo, R., B. Meyer, G. C. P. King, A. Rigo, and D. Papanastassiou (1996), Quaternary evolution of the Corinth Rift and its implications for the late Cenozoic evolution of the Aegean, *Geophys. J. Int.*, *126*, 11–53, doi:10.1111/j.1365-246X.1996.tb05264.x.

Audet, P., M. G. Bostock, N. Christensen, and S. Peacock (2009), Seismic evidence for overpressured subducted oceanic crust and megathrust fault sealing, *Nature*, *457*(7225), 76–78, doi:10.1038/nature07650.

Beaumont, C., S. Ellis, and A. Pfiffner (1999), Dynamics of sediment subduction-accretion at convergent margins: Short-term modes, long-term deformation, and tectonic implications, *J. Geophys. Res.*, *104*(B8), 17,573–17,601.

Becker, T. W., and C. Faccenna (2009), A review of the role of subduction dynamics for regional and global plate motions, in *Subduction Zone Geodynamics*, edited by S. E. Lallemand and F. Funiciello, pp. 3–34, Springer, Berlin, doi:10.1007/978-3-540-87974-9_1.

Bialas, R. W., F. Funiciello, and C. Faccenna (2011), Subduction and exhumation of continental crust: Insights from laboratory models, *Geophys. J. Int.*, *184*, 43–64, doi:10.1111/j.1365-246X.2010.04824.x.

Bohnhoff, M., J. Makris, D. Papanikolaou, and G. Stavrakakis (2001), Crustal investigation of the Hellenic subduction zone using wide aperture seismic data, *Tectonophysics*, *343*, 239–262, doi:10.1016/S0040-1951(01)00264-5.

Bostock, M. G., and S. Rondenay (1999), Migration of scattered teleseismic body waves, *Geophys. J. Int.*, *137*, 732–746, doi:10.1046/j.1365-246x.1999.00813.x.

Bostock, M. G., S. Rondenay, and J. Shragge (2001), Multiparameter two-dimensional inversion of scattered teleseismic body waves: 1. Theory for oblique incidence, *J. Geophys. Res.*, *106*(B12), 30,771–30,782, doi:10.1029/2001JB000330.

Bourova, E., I. Kassaras, H. A. Pedersen, T. Yanovskaya, D. Hatzfeld, and A. Kiratzi (2005), Constraints on absolute S velocities beneath the Aegean Sea from surface wave analysis, *Geophys. J. Int.*, *160*(3), 1006–1019, doi:10.1111/j.1365-246X.2005.02565.x.

Brun, J. P., and C. Faccenna (2008), Exhumation of high-pressure rocks driven by slab rollback, *Earth Planet. Sci. Lett.*, *272*, 1–7, doi:10.1016/j.epsl.2008.02.038.

Calcagnile, G., F. D'Ingeo, P. Farrugia, and G. F. Panza (1982), The lithosphere in the central-eastern Mediterranean area, *Pure Appl. Geophys.*, *120*(2), 389–406, doi:10.1007/BF00877044.

Carminati, E., M. J. R. Wortel, W. Spakman, and R. Sabadini (1998), The role of slab detachment processes in the opening of the western–central Mediterranean basins: Some geological and geophysical evidence, *Earth Planet. Sci. Lett.*, *160*, 651–665, doi:10.1016/S0012-821X(98)00118-6.

Cassinis, R., S. Scarascia, and A. Lozej (2003), The deep crustal structure of Italy and surrounding areas from seismic refraction data: A new synthesis, *Boll. Geofis. Teor. Appl.*, *122*, 365–375.

Chemenda, A. I., M. Mattauer, and A. N. Bokum (1996), Continental subduction and a mechanism for exhumation of high-pressure metamorphic rocks: New modelling and field data from Oman, *Earth Planet. Sci. Lett.*, *143*, 173–182, doi:10.1016/0012-821X(96)00123-9.

Clément, C., A. Hirn, P. Charvis, M. Sachpazi, and F. Marnelis (2000), Seismic structure and the active Hellenic subduction in the Ionian islands, *Tectonophysics*, *329*, 141–156, doi:10.1016/S0040-1951(00)00193-1.

Clément, C., M. Sachpazi, P. Charvis, D. Graindorge, M. Laigle, A. Hirn, and G. Zafiropoulos (2004), Reflection–refraction seismics in the Gulf of Corinth: Hints at deep structure and control of the deep marine basin, *Tectonophysics*, *391*, 97–108, doi:10.1016/j.tecto.2004.07.010.

Cruciani, C., E. Carminati, and C. Doglioni (2005), Slab dip vs. lithosphere age: No direct function, *Earth Planet. Sci. Lett.*, *238*, 298–310, doi:10.1016/j.epsl.2005.07.025.

De Franco, R., R. Govers, and M. J. R. Wortel (2008), Dynamics of continental collision: Influence of the plate contact, *Geophys. J. Int.*, *174*, 1101–1120, doi:10.1111/j.1365-246X.2008.03857.x.

de Voogd, B., C. Truffert, N. Chamot-Rooke, P. Huchon, S. Lallemant, and X. Le Pichon (1992), Two-ship deep seismic soundings in the basins of the Eastern Mediterranean Sea (Pasiphae cruise), *Geophys. J. Int.*, *109*(3), 536–552, doi:10.1111/j.1365-246X.1992.tb00116.x.

Dewey, J. F., and C. Şengör (1979), Aegean and surrounding regions: Complex multiplate and continuum tectonics in a convergent zone, *Geol. Soc. Am. Bull.*, *90*(1), 84–92, doi:10.1130/0016-7606(1979)90<84:AASRCM>2.0.CO;2.

Di Luccio, F., and M. E. Pasyanos (2007), Crustal and upper-mantle structure in the eastern Mediterranean from the analysis of surface wave dispersion curves, *Geophys. J. Int.*, *169*(3), 1139–1152, doi:10.1111/j.1365-246X.2007.03332.x.

Ellis, S., C. Beaumont, and A. Pfiffner (1999), Geodynamic models of crustal-scale episodic tectonic accretion and underplating in subduction zones, *J. Geophys. Res.*, *104*(B7), 15,169–15,190, doi:10.1029/1999JB900071.

Endrun, B., L. Ceranna, T. Meier, M. Bohnhoff, and H. P. Harjes (2005), Modeling the influence of Moho topography on receiver functions: A case study from the central Hellenic subduction zone, *Geophys. Res. Lett.*, *32*, L12311, doi:10.1029/2005GL023066.

Endrun, B., T. Meier, S. Lebedev, M. Bohnhoff, G. Stavrakakis, and H. P. Harjes (2008), S velocity structure and radial anisotropy in the Aegean region from surface wave dispersion, *Geophys. J. Int.*, *174*(2), 593–616, doi:10.1111/j.1365-246X.2008.03802.x.

Faccenna, C., and T. W. Becker (2010), Shaping mobile belts by small-scale convection, *Nature*, *465*, 602–605, doi:10.1038/nature09064.

Finetti, I. (1982), Structure, stratigraphy and evolution of central Mediterranean, *Boll. Geof. Teor. Appl.*, *24*, 247–426.

Finetti, I. R., and A. Del Ben (2005), Crustal tectono-stratigraphic setting of the Adriatic Sea from new CROP seismic data, in *CROP Project: Deep Seismic Exploration of the Central Mediterranean and Italy*, *Atlases Geosci.*, vol. 1, edited by I. R. Finetti, pp. 519–548, Elsevier, Amsterdam.

Finetti, I., D. Papanikolaou, A. Del Ben, and P. Karvelis (1991), Preliminary geotectonic interpretation of the East Mediterranean chain and the Hellenic arc, *Bull. Geol. Soc. Greece*, *25*(1), 509–526.

Frederiksen, A. W., and M. G. Bostock (2000), Modelling teleseismic waves in dipping anisotropic structures, *Geophys. J. Int.*, *141*, 401–412, doi:10.1046/j.1365-246x.2000.00090.x.

Fytikas, M., and N. P. Kolios (1979), Preliminary heat flow map of Greece, in *Terrestrial Heat Flow in Europe*, edited by V. Cermak and L. Rybach, pp. 197–205, Springer, Berlin, doi:10.1007/978-3-642-95357-6_20.

Fytikas, M., O. Giuliani, F. Innocenti, G. Marinelli, and R. Mazzuoli (1976), Geochronological data on recent magmatism of the Aegean Sea, *Tectonophysics*, *31*, T29–T34, doi:10.1016/0040-1951(76)90161-X.

Galanopoulos, D., V. Sakkas, D. Kosmatos, and E. Lagios (2005), Geoelectric investigation of the Hellenic subduction zone using long period magnetotelluric data, *Tectonophysics*, *409*, 73–84, doi:10.1016/j.tecto.2005.08.010.

Gautier, P., J. P. Brun, R. Moriceau, D. Sokoutis, J. Martinod, and L. Jolivet (1999), Timing, kinematics and cause of Aegean extension: A scenario based on a comparison with simple analogue experiments, *Tectonophysics*, *315*, 31–72, doi:10.1016/S0040-1951(99)00281-4.

Gesret, A., M. Laigle, J. Diaz, M. Sachpazi, and A. Hirn (2010), The oceanic nature of the African slab subducted under Peloponnesus: Thin-layer resolution from multiscale analysis of teleseismic *P*-to-*S* converted waves, *Geophys. J. Int.*, *183*(2), 833–849, doi:10.1111/j.1365-246X.2010.04738.x.

Gesret, A., M. Laigle, J. Diaz, M. Sachpazi, M. Charalampakis, and A. Hirn (2011), Slab tops dips resolved by teleseismic converted waves in the Hellenic subduction zone, *Geophys. Res. Lett.*, *38*, L20304, doi:10.1029/2011GL048996.

Goldsworthy, M., J. Jackson, and J. Haines (2002), The continuity of active fault systems in Greece, *Geophys. J. Int.*, *148*(3), 596–618, doi:10.1046/j.1365-246X.2002.01609.x.

Govers, R., and M. J. R. Wortel (2005), Lithosphere tearing at STEP faults: Response to edges of subduction zones, *Earth Planet. Sci. Lett.*, *236*, 505–523, doi:10.1016/j.epsl.2005.03.022.

Hacker, B. R. (2008), H$_2$O subduction beyond arcs, *Geochem. Geophys. Geosyst.*, *9*, Q03001, doi:10.1029/2007GC001707.

Hacker, B. R., and G. A. Abers (2004), Subduction Factory 3. An Excel worksheet and macro for calculating the densities, seismic wave speeds, and H$_2$O contents of minerals and rocks at pressure and temperature, *Geochem. Geophys. Geosyst.*, *5*, Q01005, doi:10.1029/2003GC000614.

Hacker, B. R., S. M. Peacock, G. A. Abers, and S. Holloway (2003), Subduction Factory 2. Intermediate-depth earthquakes in subducting slabs are linked to metamorphic dehydration reactions, *J. Geophys. Res.*, *108*(B1), 2030 doi:10.1029/2001JB001129.

Hager, B. H., and R. J. O'Connell (1978), Subduction zone dip angles and flow driven by plate motion, *Tectonophysics*, *50*, 111–133, doi:10.1016/0040-1951(78)90130-0.

Hashida, T., G. Stavrakakis, and K. Shimazaki (1988), Three-dimensional seismic attenuation structure beneath the Aegean region and its tectonic implications, *Tectonophysics*, *145*, 43–54, doi:10.1016/0040-1951(88)90314-9.

Hearn, T. M. (1999), Uppermost mantle velocities and anisotropy beneath Europe, *J. Geophys. Res.*, *104*(B7), 15,123–15,139.

Hirn, A., M. Sachpazi, R. Siliqi, J. McBride, F. Marnelis, and L. Cernobori, and the STREAMERS-PROFILES group (1996), A traverse of the Ionian islands front with coincident normal incidence and wide-angle seismics, *Tectonophysics*, *264*, 35–49, doi:10.1016/S0040-1951(96)00116-3.

Hollenstein, C., M. D. Muller, A. Geiger, and H. G. Kahle (2008), Crustal motion and deformation in Greece from a decade of GPS measurements, 1993–2003, *Tectonophysics*, *449*, 17–40, doi:10.1016/j.tecto.2007.12.006.

Hosa, A. (2008), Imaging of the Hellenic subduction zone by seismic tomography, BSc thesis, Mass. Inst. of Technol., Cambridge.

Husson, L., J. P. Brun, P. Yamato, and C. Faccenna (2009), Episodic slab rollback fosters HP-UHP rocks exhumation, *Geophys. J. Int.*, *179*(3), 1292–1300, doi:10.1111/j.1365-246X.2009.04372.x.

Kahle, H. G., and S. Mueller (1998), Structure and dynamics of the Eurasian-African/Arabian plate boundary system: Objectives, tasks and resources of the WEGENER group, *J. Geodyn.*, *25*, 303–325, doi:10.1016/S0264-3707(97)00033-1.

Kahle, H. G., M. Muller, A. Geiger, G. Danuser, S. Mueller, G. Veis, H. Billiris, and D. Paradissis (1995), The strain field in northwestern Greece and the Ionian Islands: Results inferred from GPS measurements, *Tectonophysics*, *249*, 41–52, doi:10.1016/0040-1951(95)00042-L.

Kahle, H. G., M. Cocard, Y. Peter, A. Geiger, R. Reilenger, A. Barka, and G. Veis (2000), GPS-derived strain rate field within the boundary zones of the Eurasian, African, and Arabian Plates, *J. Geophys. Res.*, *105*(B10), 23,353–23,370, doi:10.1029/2000JB900238.

Karagianni, E. E., and C. B. Papazachos (2007), Shear velocity structure in the Aegean region obtained by joint inversion of Rayleigh and Love waves, *Geol. Soc. Spec. Publ.*, *291*, 159–181, doi:10.1144/SP291.8.

Karagianni, E. E., C. B. Papazachos, D. G. Panagiotopoulos, P. Suhadolc, A. Vuan, and G. Panza (2005), Shear velocity structure in the Aegean area obtained by inversion of Rayleigh waves, *Geophys. J. Int.*, *160*(1), 127–143, doi:10.1111/j.1365-246X.2005.02354.x.

Karason, H. (2002) Constraints on mantle convection from seismic tomography and flow modeling, PhD thesis, Mass. Inst. of Technol., Cambridge.

Kennett, B. L. N. (1991), The removal of free surface interactions from three-component seismograms, *Geophys. J. Int.*, *104*, 153–154, doi:10.1111/j.1365-246X.1991.tb02501.x.

Knapmeyer, M., and H. Harjes (2000), Imaging crustal discontinuities and the downgoing slab beneath western Crete, *Geophys. J. Int.*, *143*(1), 1–21, doi:10.1046/j.1365-246x.2000.00197.x.

Kokinou, E., A. Vafidis, M. Loucogiannakis, and I. Louis (2003), Deep seismic imaging and velocity estimation in Ionian Sea, *J. Balkan Geophys. Soc.*, *6*(2), 100–116.

Kokinou, E., E. Kamberis, A. Vafidis, D. Monopolis, G. Ananiadis, and A. Zelilidis (2005), Deep seismic reflection data from offshore western Greece: A new crustal model for the Ionian sea, *J. Pet. Geol.*, *28*(2), 185–202, doi:10.1111/j.1747-5457.2005.tb00079.x.

Konstantinou, K. I., and N. S. Melis (2008), High-frequency shear-wave propagation across the Hellenic subduction zone, *Bull. Seismol. Soc. Am.*, *98*(2), 797–803, doi:10.1785/0120060238.

Kopf, A., J. Mascle, and D. Klaeschen (2003), The Mediterranean Ridge: A mass balance across the fastest growing accretionary complex on Earth, *J. Geophys. Res.*, *108*(B8), 2372, doi:10.1029/2001JB000473.

Lallemand, S., A. Heuret, and D. Boutelier (2005), On the relationships between slab dip, backarc stress, upper plate absolute motion, and crustal nature in subduction zones, *Geochem. Geophys. Geosyst.*, *6*, Q09006, doi:10.1029/2005GC000917.

Le Pichon, X., and J. Angelier (1979), The Hellenic arc and trench system: A key to the neotectonic evolution of the eastern Mediterranean area, *Tectonophysics*, *60*, 1–42, doi:10.1016/0040-1951(79)90131-8.

Li, X., G. Bock, A. Vafidis, R. Kind, H. P. Harjes, W. Hanka, K. Wylegalla, M. van der Meijde, and X. Yuan (2003), Receiver function study of the Hellenic subduction zone: Imaging crustal thickness variations and the oceanic Moho of the descending African lithosphere, *Geophys. J. Int.*, *155*(2), 733–748, doi:10.1046/j.1365-246X.2003.02100.x.

Ligdas, C. N., I. G. Main, and R. D. Adams (1990), 3-D structure of the lithosphere in the Aegean region, *Geophys. J. Int.*, *102*(1), 219–229, doi:10.1111/j.1365-246X.1990.tb00543.x.

MacKenzie, L. M., G. A. Abers, S. Rondenay, and K. M. Fischer (2010), Imaging a steeply dipping subducting slab in southern Central America, *Earth Planet. Sci. Lett.*, *296*, 459–468, doi:10.1016/j.epsl.2010.05.033.

Makris, J. (1985), Geophysics and geodynamic implications for the evolution of the Hellenides, in *Geological Evolution of the Mediterranean Basin*, edited by D. J. Stanley and F. Wezel, pp. 231–248, Springer, Berlin, doi:10.1007/978-1-4613-8572-1_11.

Marone, F., M. van der Meijde, S. van der Lee, and D. Giardini (2003), Joint inversion of local, regional and teleseismic data for crustal thickness in the Eurasia-Africa plate boundary region, *Geophys. J. Int.*, *154*(2), 499–514, doi:10.1046/j.1365-246X.2003.01973.x.

Martínez, M. D., J. A. Canas, X. Lana, and J. Badal (2001), Objective regionalization of Rayleigh wave dispersion data by clustering algorithms: An application to the Mediterranean basin, *Tectonophysics*, *330*, 245–266, doi:10.1016/S0040-1951(00)00231-6.

Mascle, J., and E. Chaumillon (1998), An overview of Mediterranean Ridge collisional accretionary complex as deduced from multichannel seismic data, *Geo Mar. Lett.*, *18*(2), 81–89, doi:10.1007/s003670050056.

McClusky, S., et al. (2000), Global Positioning System constraints on plate kinematics and dynamic in the eastern Mediterranean and Caucasus, *J. Geophys. Res.*, *105*(B3), 5695–5719, doi:10.1016/j.tecto.2007.12.006.

McKenzie, D. (1972), Active tectonics of the Mediterranean region, *Geophys. J. R. Astron. Soc.*, *30*(2), 109–185, doi:10.1111/j.1365-246X.1972.tb02351.x.

Meier, T., M. Rische, B. Endrun, A. Vafidis, and H. P. Harjes (2004), Seismicity of the Hellenic subduction zone in the area of western and central Crete observed by temporary local seismic networks, *Tectonophysics*, *383*, 149–169, doi:10.1016/j.tecto.2004.02.004.

Meijer, P. T., and M. J. R. Wortel (1996), Temporal variation in the stress field of the Aegean region, *Geophys. Res. Lett.*, *23*(5), 439–442.

Mercier, J. L., D. Sorel, P. Vergely, and K. Simeakis (1989), Extensional tectonic regimes in the Aegean basins during the Cenozoic, *Basin Res.*, *2*(1), 49–71, doi:10.1111/j.1365-2117.1989.tb00026.x.

Meyer, B., R. Armijo, and D. Dimitrov (2002), Active faulting in SW Bulgaria: Possible surface rupture of the 1904 Struma earthquakes, *Geophys. J. Int.*, *148*, 246–255.

Miller, D., M. Oristaglio, and G. Beylkin (1987), A new slant on seismic imaging: Migration and integral geometry, *Geophysics*, *52*(7), 943–964.

Monopolis, D., and A. Bruneton (1982), Ionian sea (western Greece): Its structural outline deduced from drilling and geophysical data, *Tectonophysics*, *83*, 227–242, doi:10.1016/0040-1951(82)90020-8.

Morelli, C., C. Gantar, and M. Pisani (1975), Bathymetry, gravity and magnetism in the Strait of Sicily and in the Ionian Sea, *Boll. Geofis. Teor. Appl.*, *17*, 39–58.

Moretti, I., and L. H. Royden (1988), Deflection, gravity anomalies and tectonics of doubly subducted continental lithosphere: Adriatic and Ionian seas, *Tectonics*, *7*(4), 875–893, doi:10.1029/TC007i004p00875.

Papanikolaou, D. (1993), Geotectonic evolution of the Aegean, *Bull. Soc. Geol. Greece*, *28*(1), 33–48.

Papanikolaou, D. (2009), Timing of tectonic emplacement of the ophiolites and terrane paleogeography of the Hellenides, *Lithos*, *108*, 262–280, doi:10.1016/j.lithos.2008.08.003.

Papanikolaou, D., and L. Royden (2007), Disruption of the Hellenic arc: Late Miocene extensional detachment faults and steep Pliocene-Quaternary normal faults—Or what happened at Corinth?, *Tectonics*, *26*, TC5003, doi:10.1029/2006TC002007.

Papazachos, B. C., V. E. Karakostas, C. B. Papazachos, and E. M. Scordilis (2000), The geometry of the Wadati–Benioff zone and lithospheric kinematics in the Hellenic arc, *Tectonophysics*, *319*(4), 275–300, doi:10.1016/S0040-1951(99)00299-1.

Papazachos, C., and G. Nolet (1997), P and S deep velocity structure of the Hellenic area obtained by robust nonlinear inversion of travel times, *J. Geophys. Res.*, *102*(B4), 8349–8367, doi:10.1029/96JB03730.

Papazachos, C. B., P. M. Hatzidimitriou, D. G. Panagiotopoulos, and G. N. Tsokas (1995), Tomography of the crust and upper mantle in southeast Europe, *J. Geophys. Res.*, *100*(B7), 12,405–12,422, doi:10.1029/95JB00669.

Pasyanos, M. E., and W. R. Walter (2002), Crust and upper-mantle structure of North Africa, Europe and the Middle East from inversion of surface waves, *Geophys. J. Int.*, *149*(2), 463–481, doi:10.1046/j.1365-246X.2002.01663.x.

Pe-Piper, G., and D. J. W. Piper (2007), Neogene backarc volcanism of the Aegean: New insights into the relationship between magmatism and tectonics, *Spec. Pap. Geol. Soc. Am.*, *418*, 17–31.

Piromallo, C., and A. Morelli (2003), P wave tomography of the mantle under the Alpine-Mediterranean area, *J. Geophys. Res.*, *108*(B2), 2065, doi:10.1029/2002JB001757.

Reilinger, R., S. McClusky, D. Paradissis, S. Ergintav, and P. Vernant (2010), Geodetic constraints on the tectonic evolution of the Aegean region and strain accumulation along the Hellenic subduction zone, *Tectonophysics*, *488*, 22–30, doi:10.1016/j.tecto.2009.05.027.

Roberts, S., and J. Jackson (1991), Active normal faulting in central Greece: An overview, *Geol. Soc. Spec. Publ.*, *56*(1), 125–142, doi:10.1144/GSL.SP.1991.056.01.09.

Rondenay, S. (2009), Upper mantle imaging with array recordings of converted and scattered teleseismic waves, *Surv. Geophys.*, *30*, 377–405, doi:10.1007/s10712-009-9071-5.

Rondenay, S., M. G. Bostock, and J. Shragge (2001), Multiparameter two-dimensional inversion of scattered teleseismic body waves: 3. Application to the Cascadia 1993 data set, *J. Geophys. Res.*, *106*(B12), 30,795–30,807, doi:10.1029/2000JB000039.

Rondenay, S., M. G. Bostock, and K. Fischer (2005), Multichannel inversion of scattered teleseismic body waves: Practical considerations and applicability, in *Seismic Earth: Array Analysis of Broadband Seismograms*, *Geophys. Monogr. Ser.*, vol. 157, edited by A. Levander and G. Nolet, pp. 187–203, AGU, Washington, D. C., doi:10.1029/157GM12.

Rondenay, S., G. A. Abers, and P. van Keken (2008), Seismic imaging of subduction zone metamorphism, *Geology*, *36*(4), 275–278, doi:10.1130/G24112A.1.

Rondenay, S., L. G. J. Montési, and G. A. Abers (2010), New geophysical insight into the origin of the Denali volcanic gap, *Geophys. J. Int.*, *182*, 613–630, doi:10.1111/j.1365-246X.2010.04659.x.

Royden, L. H. (1993), The tectonic expression of slab pull at continental convergent boundaries, *Tectonics*, *12*, 303–325, doi:10.1029/92TC02248.

Royden, L. H., and L. Husson (2006), Trench motion, slab geometry and viscous stresses in subduction systems, *Geophys. J. Int.*, *167*, 881–905, doi:10.1111/j.1365-246X.2006.03079.x.

Royden, L. H., and L. Husson (2009), Subduction with variations in slab buoyancy: Models and application to the Banda and Apennine systems, in *Subduction Zone Geodynamics*, edited by S. E. Lallemand and F. Funiciello, pp. 35–45, Springer, Berlin, doi:10.1007/978-3-540-87974-9_2.

Royden, L. H., and D. Papanikolaou (2011), Slab segmentation and late Cenozoic disruption of the Hellenic arc, *Geochem. Geophys. Geosyst.*, *12*, Q03010, doi:10.1029/2010GC003280.

Sachpazi, M., A. Galvé, M. Laigle, A. Hirn, E. Sokos, A. Serpetsidaki, J.-M. Marthelot, J. M. Pi Alperin, B. Zelt, and B. Taylor (2007), Moho topography under central Greece and its compensation by Pn time-terms for the accurate location of hypocenters: The example of the Gulf of Corinth 1995 Aigion earthquake, *Tectonophysics*, *440*, 53–65, doi:10.1016/j.tecto.2007.01.009.

Schmid, C., S. van der Lee, and D. Giardini (2004), Delay times and shearwave splitting in the Mediterranean region, *Geophys. J. Int.*, *159*(1), 275–290, doi:10.1111/j.1365-246X.2004.02381.x.

Schmid, C., S. van der Lee, and D. Giardini (2006), Correlated shear and bulk moduli to 1400 km beneath the Mediterranean region, *Phys. Earth Planet. Inter.*, *159*, 213–224, doi:10.1016/j.pepi.2006.07.003.

Sengor, A. M. C., N. Gorur, and F. Saroglu (1985), Strike-slip faulting and related basin formation in zones of tectonic escape: Turkey as a case study, in *Strike-Slip Faulting and Basin Formation*, edited by K. T. Biddle and N. Christie-Blick, *Spec. Publ. Soc. Econ. Paleontol. Mineral.*, *37*, 227–264.

Shragge, J., M. G. Bostock, and S. Rondenay (2001), Multiparameter two-dimensional inversion of scattered teleseismic body waves: 2. Numerical examples, *J. Geophys. Res.*, *106*(B12), 30,783–30,793, doi:10.1029/2001JB000326.

Sodoudi, F., R. Kind, D. Hatzfeld, K. Priestley, W. Hanka, K. Wylegalla, G. Stavrakakis, A. Vafidis, H. P. Harjes, and M. Bohnhoff (2006), Lithospheric structure of the Aegean obtained from P and S receiver functions, *J. Geophys. Res.*, *111*, B12307, doi:10.1029/2005JB003932.

Spakman, W., M. J. R. Wortel, and N. J. Vlaar (1988), The Hellenic subduction zone: A tomographic image and its geodynamic implications, *Geophys. Res. Lett.*, *15*(1), 60–63, doi:10.1029/GL015i001p00060.

Spakman, W., S. van der Lee, and R. van der Hilst (1993), Travel-time tomography of the European-Mediterranean mantle down to 1400 km, *Phys. Earth Planet. Inter.*, *79*, 3–74, doi:10.1016/0031-9201(93)90142-V.

Suckale, J., S. Rondenay, M. Sachpazi, M. Charalampakis, A. Hosa, and L. H. Royden (2009), High-resolution seismic imaging of the western Hellenic subduction zone using teleseismic scattered waves, *Geophys. J. Int.*, *178*(2), 775–791, doi:10.1111/j.1365-246X.2009.04170.x.

Syracuse, E. M., P. E. van Keken, and G. A. Abers (2010), The global range of subduction zone thermal models, *Phys. Earth Planet. Inter.*, *51*(8), 1761–1782, doi:10.1016/j.pepi.2010.02.004.

Taymaz, T., J. Jackson, and D. McKenzie (1991), Active tectonics of the north and central Aegean Sea, *Geophys. J. Int.*, *106*, 433–490, doi:10.1111/j.1365-246X.1991.tb03906.x.

Tiberi, C., et al. (2000), Crustal and upper mantle structure beneath the Corinth rift (Greece) from a teleseismic tomography study, *J. Geophys. Res.*, *105*(B12), 28,159–28,171, doi:10.1029/2000JB900216.

Tiberi, C., M. Diament, H. Lyon-Caen, and T. King (2001), Moho topography beneath the Corinth Rift area (Greece) from inversion of gravity data, *Geophys. J. Int.*, *145*(3), 797–808, doi:10.1046/j.1365-246x.2001.01441.x.

Tirel, C., F. Gueydan, C. Tiberi, and J. P. Brun (2004), Aegean crustal thickness inferred from gravity inversion. Geodynamical implications, *Earth Planet. Sci. Lett.*, *228*, 267–280, doi:10.1016/j.epsl.2004.10.023.

Tsokas, G. N., and R. O. Hansen (1997), Study of the crustal thickness and the subducting lithosphere in Greece from gravity data, *J. Geophys. Res.*, *102*(B9), 20,585–20,597.

VanDecar, J. C., and R. S. Crosson (1990), Determination of teleseismic relative phase arrival times using multi-channel cross-correlation and least squares, *Bull. Seismol. Soc. Am.*, *80*, 150–159.

van der Hilst, R. D., S. Widiyantoro, and E. R. Engdahl (1997), Evidence for deep mantle circulation from global tomography, *Nature*, *386*(6625), 578–584, doi:10.1038/386578a0.

van der Meijde, M., S. van der Lee, and D. Giardini (2003), Crustal structure beneath broad-band seismic stations in the Mediterranean region, *Geophys. J. Int.*, *152*(3), 729–739, doi:10.1046/j.1365-246X.2003.01871.x.

van Hinsbergen, D. J. J., E. Hafkenscheid, W. Spakman, J. E. Meulenkamp, and M. J. R. Wortel (2005), Nappe stacking resulting from subduction of oceanic and continental lithosphere below Greece, *Geology*, *33*(4), 325–328, doi:10.1130/G20878.1.

van Keken, P. E., B. R. Hacker, E. M. Syracuse, and G. A. Abers (2011), Subduction factory: 4. Depth-dependent flux of H_2O from subducting slabs worldwide, *J. Geophys. Res.*, *116*, B01401, doi:10.1029/2010JB007922.

Vassilakis, E., L. Royden, and D. Papanikolaou (2011), Kinematic links between subduction along the Hellenic trench and extension in the Gulf of Corinth, Greece: A multidisciplinary analysis, *Earth Planet. Sci. Lett.*, *303*, 108–120, doi:10.1016/j.epsl.2010.12.054.

Wada, I., and K. L. Wang (2009), Common depth of slab-mantle decoupling: Reconciling diversity and uniformity of subduction zones, *Geochem. Geophys. Geosyst.*, *10*, Q10009, doi:10.1029/2009GC002570.

Warren, C. J., C. Beaumont, and R. A. Jamieson (2008), Modelling tectonic styles and ultra-high pressure (UHP) rock exhumation in the transition from oceanic subduction to continental collision, *Earth Planet. Sci. Lett.*, *267*, 129–145, doi:10.1016/j.epsl.2007.11.025.

Waschbusch, P., and C. Beaumont (1996), Effect of slab retreat on crustal deformation in simple regions of plate convergence, *J. Geophys. Res.*, *101*, 28,133–28,148, doi:10.1029/96JB02482.

Wortel, M. J. R., and W. Spakman (2000), Subduction and Slab Detachment in the Mediterranean-Carpathian Region, *Science*, *290*(5498), 1910–1917, doi:10.1126/science.290.5498.1910.

Zelt, B. C., B. Taylor, M. Sachpazi, and A. Hirn (2005), Crustal velocity and Moho structure beneath the Gulf of Corinth, Greece, *Geophys. J. Int.*, *162*(1), 257–268, doi:10.1111/j.1365-246X.2005.02640.x.

Zhu, L. P., B. J. Mitchell, N. Akyol, I. Cemen, and K. Kekovali (2006), Crustal thickness variations in the Aegean region and implications for the extension of continental crust, *J. Geophys. Res.*, *111*, B01301, doi:10.1029/2005JB003770.